- 1 Footwall refrigeration versus footwall hydration: Reassessing steep thermal gradients below
- 2 detachment faults with *in situ* SIMS oxygen isotope analysis

4 Claudia I. Roig González^{1*}, Chloë Bonamici¹, Tyler Blum¹, William O. Nachlas¹

- 6 1. Department of Geoscience, University of Wisconsin-Madison, Madison, WI, United States.
- 7 Corresponding author: roig@wisc.edu

Abstract

The extensional detachment systems of metamorphic core complexes (MCC) have the potential to facilitate significant fluid movement between Earth's surface and the warm, ductile middle crust. One long-standing and influential detachment fault-fluid interaction model called the "footwall refrigeration hypothesis" (Morrison and Anderson, 1998) postulates that cool meteoric fluids circulating downward along a detachment can facilitate large-scale heat loss at depth before rocks are exhumed by faulting. Stable isotopes of oxygen and hydrogen have long been recognized as potentially useful tracers of surface-to-depth fluid flow in core complexes; however, typical sampling methods and the competing effects between temperature and fluid composition have made oxygen isotope signatures of meteoric fluid infiltration difficult to detect and/or interpret in the rock record.

Here, we use in situ δ^{18} O measurements by secondary ion mass spectrometry (SIMS) to address the rock record of meteoric fluid interactions and temperature variation within the Whipple Mountains MCC footwall beneath the Whipple detachment fault (WDF). The microscale sampling of SIMS (10 μ m diameter x 1-2 μ m deep pits) allows investigation of isotope

variability as a function of mineral geochemistry and microstructure and enables more accurate interpretation of the causes of isotope variability. In the Whipple footwall mylonites, quartz and epidote show grain-to-grain oxygen-isotope variability within samples and as a function of distance from the main detachment. Approaching the WDF, both quartz and epidote show increasing spread toward low δ^{18} O values. The lowest SIMS-measured δ^{18} O epidote values require exchange with a low δ^{18} O, meteoric fluid at high temperature. However, SIMS data also reveal that meteoric fluid-rock interactions were spatially heterogeneous at the scale of individual grains, resulting in local preservation of metamorphic quartz-epidote oxygen isotope equilibrium unaffected by infiltrating meteoric fluid. Within preserved metamorphic domains at all investigated structural levels of the WDF footwall, quartz and epidote δ^{18} O values are tightly clustered and yield similar fractionations (Δ^{18} O_{qz-ep}). For samples from the longest footwall traverse, these Δ^{18} O_{qz-ep} values are $4.0 \pm 0.4\%$, consistent with δ^{18} O equilibrium at $521 \pm 43/-37$ °C. We conclude that there is no evidence of a large paleo-thermal gradient associated with the Whipple Detachment Fault (i.e., no evidence for footwall refrigeration).

Keywords: Whipple Detachment Fault, SIMS, oxygen isotopes, metamorphic core complex,

fluid-rock interactions, thermometry, mylonites

1. Introduction

The fault systems of metamorphic core complexes have long been suspected to facilitate infiltration of meteoric fluids to midcrustal depths (Fricke et al., 1992; Gébelin et al., 2015; Gottardi et al., 2018; Losh, 1997; McCaig, 1989; Methner et al., 2015; Person et al., 2007). The well-known weakening effects of fluids in deforming rocks (e.g. Gottardi and Hughes, 2022;

Kronenberg, 1994), along with the temperature contrast between cool surface fluids and the warm middle crust, suggests a high potential for thermomechanical feedbacks in detachment fault systems infiltrated by meteoric water (e.g., Gottardi et al., 2011). For instance, Selverstone et al., (2012) showed that fluid infiltration-driven reactions and mineralogical changes can localize deformation in detachment fault systems and transiently increase fluid pressures. Several other studies similarly suggest that fault-induced permeability enhances fluid flow, which then alters crustal rheological properties and promotes further faulting (Block and Royden, 1990; Coney, 1980; Fricke et al., 1992; Gottardi and Teyssier, 2013; Haines et al., 2016; Lister and Davis, 1989; McCaig et al., 1990; Morrison and Anderson, 1998; Platt et al., 2015; Sibson, 2000; Singleton and Mosher, 2012; Tirel et al., 2008; Whitney et al., 2013).

A long-standing fluid-fault interaction model developed in the Whipple Mountains metamorphic core complex (Fig. 1), is that flux of meteoric fluids along extensional detachment faults can drive rapid cooling of footwall rocks (Morrison and Anderson, 1998). This "footwall refrigeration hypothesis" effectively predicts the downward displacement of the major heat loss boundary of the deforming system from the surface of the Earth to the detachment surface, several km or more below the surface. The expected result would be telescoping of isotherms beneath the detachment fault and development of a steep thermal gradient in the detachment footwall (Fig. 1). Morrison and Anderson (1998) developed the footwall refrigeration hypothesis on the basis of an apparent paleo-thermal gradient, which they recognized by performing oxygen isotope thermometry along a 50-m depth transect into the footwall beneath the Whipple detachment fault (WDF). The paleo-thermal gradient was delineated by systematic variations in oxygen isotope fractionation between coexisting quartz and epidote with structural distance from the detachment fault. They interpreted these oxygen isotope fractionations to reflect temperature-

controlled equilibrium oxygen isotope partitioning between quartz and epidote over a range of depth (Morrison and Anderson, 1998). The temperatures calculated by oxygen isotope thermometry suggested a very large thermal gradient of ~2 °C/m in the detachment footwall, which led Morrison and Anderson (1998) to argue for efficient cooling of the footwall due to advective removal of heat by infiltrating meteoric fluids.

The Morrison and Anderson (1998) footwall refrigeration hypothesis has several implications for detachment mechanics and exhumation records. One is that rapid heat removal along and near the detachment would be expected to shut down crystal-plastic deformation in footwall mylonites (e.g., Gottardi and Teyssier, 2013) as soon as mylonites are captured by a through-going brittle detachment fault system (Davis et al., 1988; Singleton and Mosher, 2012). Another is that the detachment zone could experience high fluid pressures, which make slip on low-angle fault surfaces more favorable (Axen, 1992), from downward meteoric water infiltration alone with or without the incorporation of upward flow of deep metamorphic or magmatic fluids. Finally, the footwall refrigeration hypothesis implies footwall rocks could cool at depth prior to exhumation so that cooling inferred from thermochronometry cannot be directly related to detachment footwall exhumation (e.g., Gottardi et al., 2013; Singleton et al., 2014). This could introduce considerable uncertainty into interpretations of tectonic exhumation histories.

Previous studies have tried to understand the extent of fluid infiltration in detachment faults and its preservation in the rock isotope record. While δ^2H has provided a clear record of meteoric fluid infiltration at depth (e.g., Dusséaux et al., 2019; Gébelin et al., 2012; Gébelin et al., 2015; Gottardi et al., 2011; Gottardi et al., 2015; Gramblin et al., 2021; McFadden et al., 2015; Quilichini et al., 2015; Quilichini et al., 2016), hydrogen isotopes are insensitive to

fluid:rock ratios and cannot readily answer questions about how much fluid acted on detachment faults. Unambiguous δ^{18} O signatures of meteoric fluid infiltration are rare or highly localized in MCC rocks (e.g. Brown, 2015; Fricke et al., 1992; Person et al. 2007) because the widely used δ^{18} O measurement approaches tend to convolve the effects of temperature, fluid composition, and fluid abundance. All previously published isotopic studies of metamorphic core complexes have measured δ^{18} O on bulk rock or mineral separates, and thus have had limited ability to interrogate δ^{18} O at the grain or intragrain scales, where information about deformation and recrystallization in dynamic detachment systems can be preserved. Secondary ion mass spectrometry (SIMS) δ^{18} O techniques allow us to revisit the Morrison and Anderson (1998) study with *in situ* SIMS δ^{18} O measurements, targeting specific domains within each grain. This work applies a combination of characterization methods in conjunction with SIMS to (1) locate δ^{18} O signatures of fluid-rock interaction within grains and in microstructural context; (2) evaluate whether quartz-epidote oxygen isotope fractionations reflect thermal equilibrium; and (3) reassess evidence for the thermal gradient beneath the Whipple detachment fault.

2. Geologic Setting of Study

The Oligo-Miocene Whipple Mountain MCC in southeastern California is one of the largest MCCs (50–125-km-wide) in the Colorado River extensional corridor (Fig. 2). The lower plate rocks, which are exposed in the Whipple Mountains west of the Colorado River, consist of interlayered Proterozoic gneisses and amphibolites intruded by Cretaceous and syn-extensional Oligo-Miocene granitoids (Anderson and Cullers, 1988; Behr and Platt, 2011 and mapping compiled therein; Wooden et al., 2017; Wright, 1986). The eastern footwall rocks, making up the main topographic expression of the Whipple Mountains, are mylonitic, whereas the

topographically lower, western half of the range is non-mylonitic and contains abundant brittle faults, as well as the Miocene Chamberlain Dike Swarm (Gans and Gentry, 2016). The lower plate is ringed by intensely faulted and variably tilted upper plate rocks consisting of syndeformational Tertiary volcanic and sedimentary strata, as well as slices of Proterozoic gneiss (Davis and Anderson 1991; Davis et al., 1980; Yin and Dunn, 1992).

116

117

118

119

120

121

122

123

124

125

126

127

128

129

130

131

132

133

134

135

136

137

138

The Whipple detachment fault (WDF) is a low-angle normal fault that accommodated 40-50 km of top-NE extension between 26 and 16 Ma (Davis et al., 1986). The detachment footwall mylonite zone was brittlely overprinted during exhumation through the brittle-ductile transition, creating a breccia zone up to 300 m thick locally (Anderson et al., 1988; Axen and Selverstone, 1994; Beratan, 1991; Block and Royden, 1990; Davis, 1988; Davis et al., 1986; Dorsey and Becker, 1995; Morrison and Anderson, 1998). Conditions of mylonitization and brittle overprinting are constrained by multiple thermometry and thermobarometry approaches. Twofeldspar thermometry indicates mylonitization at 458 ± 35 °C in the shallow footwall, increasing with depth to $535 \pm 44^{\circ}$ (Anderson et al., 1988; Davis et al., 1980). More recent Ti-in-quartz thermometry corroborates upper mylonitization temperatures >500 °C but extends the lower temperature range to 308 ± 40 °C (Behr and Platt, 2011). Fluid inclusions analysis and phase equilibria modeling of subdetachment shear zones within the footwall gives deformation temperature of 350-450 °C (Selverstone et al., 2012). The exact timing of the onset of the footwall rock mylonitization is unknown, but U-Pb dating of igneous intrusive suites within the Whipple Mountain MCC constrain it to ≤ 26 Ma (e.g. Anderson et al., 1981). Ar-Ar hornblende from Proterozoic and Cretaceous gneisses (Anderson, 1988); U/Th-He apatite and zircon (Stockli et al., 2006); and Ar-Ar hornblende, plagioclase, and biotite (Gans and Gentry, 2016), as well as U-Pb zircon dates, from the syn-extensional Chamberlain Wells Dike Swarm (Gans and Gentry,

2016) suggest continued deformation, exhumation and cooling between 20 Ma and 13 Ma.

3. Sampling and Methods

3.1 Sample collection

We report data from five mylonitic footwall rock samples collected from different structural depths (Z_{det}) below the WDF (Fig. 2). These show a range of brittle and ductile deformation macrostructures, as well as evidence of greenschist-facies metamorphism. Three samples of mylonitic Proterozoic orthogneiss (Behr and Platt, 2011) were collected along the Cupcake Mountain Trail (WM-20-8, WM-20-2 and WM-20-5), which provides access to the WDF beneath two klippen of volcanic upper plate rocks (Fig. 2). The WDF along the Cupcake Mountain Trail is a sharp contact marked by a ~ 2 m of dark green-brown cataclastic breccia. Two protomylontic granitoids (WM-20-16, WM-20-17) were collected from a similar structural depth below the WDF in Bowman's Wash, near the site of the original Morrison and Anderson (1998) study (Table 1; Fig. 2). The WDF at the Bowman's Wash sample site is marked by a cataclasite breccia ledge 1-5 m tall immediately below dark brown hanging wall volcanic rocks. Footwall rocks for several tens of meters below the detachment are protomylonitic Cretaceous granodiorite (mapping published in Behr and Platt, 2011) that contain abundant epidote and chlorite, especially in crosscutting veins and fractures.

Sample WM-20-8 is a quartzofeldspathic mylonite clast from within a well-indurated fault breccia immediately below the WDF at $Z_{det} < 1m$. The breccia consists of randomly oriented mylonitic clasts, ranging from < 1 cm to ~ 50 cm in length, within a chlorite- and epidote-rich matrix (Fig. 3A). Sample WM-20-2 is an epidote and K-feldspar porphyroclastic

mylonitic gneiss collected from the limb of a mesoscale fold (Fig. 3B) located at Z_{det} = 6m. The sample matrix consists primarily of fine-grained quartz and feldspar and includes a sharp contact zone between the quartzofeldspathic matrix and a chlorite and epidote-rich matrix. Secondary veins and fractures filled with carbonate crosscut the mylonitic fabric. Sample WM-20-16 is a biotite-epidote granitoid with a shallowly dipping protomylonitic fabric. It was collected from a jointed exposure at Z_{det} = 24m in Bowman's Wash (Fig. 3C). Sample WM-20-17 is a biotite and epidote medium-grained granitoid with a shallowly dipping protomylonitic fabric (Fig. 3D) crosscut by epidote-filled veins sampled at Z_{det} = 26m. Sample WM-20-5, collected along the Cupcake Mountain Trail at Z_{det} = 40m (Fig. 3E), is a feldspar- and epidote-porphyroclastic mylonite gneiss with millimeter- to centimeter-scale layering. Feldspar porphyroclasts are up to 1 cm in length, whereas smaller epidote porphyroclasts are typically 0.5-5 mm in diameter.

3.2 Petrologic and chemical analysis of quartz and epidote

Samples were prepared as thick sections with SIMS standard materials pre-embedded in the billets and characterized by light microscopy and secondary electron microscopy (SEM). Sections were then trimmed into SIMS-compatible, 1-inch rounds centered on target phases and microstructures of interest (See Supplemental Material Fig. S1). Petrographic analysis was coupled with SEM backscattered electron (BSE) and cathodoluminescence imaging (CL) to characterize quartz and epidote microstructural context and chemical zoning. Epidote porphyroclasts were analyzed by energy dispersive spectroscopy (EDS) prior to electron probe microanalysis (EPMA) and SIMS analysis, to identify phases and qualitatively assess chemical zoning. EPMA analyses were performed at the UW-Madison Department of Geoscience Electron Microbeam Laboratories on a CAMECA SX-FIVE electron microprobe operated at 15 kV

accelerating voltage and 20 nA beam current with a 5 μ m diameter beam. The EPMA routine included analysis of 15 elements (Na, Si, Al, Mg, Fe, Mn, Ca, Ti, La, Ce, K, Y, Nd, Sm, O) to fully characterize both epidote and the REE-rich cores (allanite) that occur in most porphyroclasts. EPMA measurements were used to calculate mole fraction epidote (X_{ep}) and correct SIMS data for compositional variations, which induce SIMS δ^{18} O instrumental bias primarily as a function of variations in Al-Fe³⁺ coupled substitution (Dessimov, 2011; Roig González, 2023). Details of EPMA methods are included in Supplementary Table 1 and elemental data and epidote mole fraction calculations are reported in Supplemental Table 2.

3.3 SIMS analysis of quartz and epidote

After chemical characterization, thin section rounds were mounted for in situ oxygen isotope analysis by SIMS on a CAMECA IMS-1280 instrument in the WiscSIMS Lab. Quartz and epidote data for Whipple samples were collected over two analytical sessions. During both sessions, the analytical protocol for obtaining high-precision $\delta^{18}O$ analyses was similar to that outlined in Kita et al., (2009) with the addition of OH/O monitoring (Wang et al., 2014). Sputtering was performed with a 1.85-2.0 nA Cs+ primary beam accelerated to 20 keV total impact energy, producing analysis pits 10 μ m in diameter and < 2 μ m deep. Surface charging was compensated with the electron gun. Secondary ion optics were tuned for mass resolution power of ~5000, and the magnetic field was stabilized by NMR. Secondary ions at masses 16, 17 ($^{16}O^{1}H$), and 18 were measured simultaneously by multicollector Faraday cups with 10^{10} , 10^{11} , and 10^{11} ohm resistors, respectively.

Analysis of quartz was calibrated with WiscSIMS quartz δ^{18} O standard UWQ-1 (Kelly et al., 2007), which was also embedded in all sample mounts as the running standard. Groups of 10-

15 sample unknown analyses were bracketed by sets of four UWQ-1 analyses to track analytical precision, instrumental bias, and instrumental drift. The 2SD reproducibility of the UWQ-1 standard, the preferred measure of total internal and external analytical uncertainty, ranged from 0.08-0.37‰, with a mean of 0.20‰. For epidote, the instrumental bias varies as a function of iron content (Roig González et al., 2023). To generate accurate measurement of δ^{18} O epidote unknowns, mass bias between epidote and running standard UWQ-1 was corrected based on a a piece-wise linear curve fit17 epidote δ^{18} O standards covering the range X_{ep} 0-0.94 (Supplemental Fig S7; Roig González et al., 2023). Each SIMS analysis was corrected according to the correlated X_{Ep} measured during EPMA analysis. EPMA spot selection was coupled with SIMS pit selection using QGIS software (e.g., Linzmeier et al., 2018) to ensure that chemical data matched the δ^{18} O isotopic data from the target area of the analyzed grains. SIMS pit inspection and imaging was performed by SEM to identify spot analyses compromised by intersection with voids, cracks or inclusions (See Supplemental Material Fig. S5). All SIMS data are reported in Supplementary Data Table 3-7 with final δ^{18} O values reported in %VSMOW.

4. Results

4.1 Mineral assemblages, microstructures, and epidote petrogenesis

Samples along the Cupcake Mountain Trail traverse (WM-20-8, WM-20-2 and WM-20-5) exhibit shallowly dipping mylonitic fabrics defined by elongate quartz ribbons, aligned biotite, and elongate feldspar porphyroclasts (Fig. 4A-F). These mylonites have the mineral assemblage epidote + biotite + quartz + feldspar + Fe-Ti oxides + titanite, with chlorite present as a widespread retrograde phase. Quartz is present as elongate aggregates and ribbons of fine grains

~10-50 µm in diameter. Larger relict quartz grains (~100-200 µm long) show undulose extinction and subgrain development, indicating subgrain rotation recrystallization as the dominant deformation mechanism (Hirth and Tullis, 1992). Feldspars, both K-feldspar and plagioclase, occur primarily as porphyroclasts with recrystallized tails, ranging from <1 mm to >1 cm in diameter. Biotite mantles porphyroclasts and is aligned with quartz ribbons defining the foliation. Samples from the Cupcake Mountain Trail contain epidote predominantly as subrounded porphyroclasts (Fig. 4A-C;F). Epidote porphyroclasts commonly show distinct core and rim chemical zones with irregular, diffuse, boundaries (Figs. 4H,I; 5A,B,C,F) (Also see Supplemental Material Fig. S2). In samples WM-20-8, WM-20-2 and WM-20-5, chlorite occurs as both an alteration of biotite and within crosscutting secondary veins and is particularly prevalent in the fractured and brecciated samples immediately below the detachment.

Samples WM-20-16 and WM-20-17 from Bowman's Wash are granodiorite with a weak, variably developed, protomylonitic fabric (Fig. 4G-J). The inferred magmatic assemblage included quartz + plagioclase + K-feldspar + biotite + allanite + apatite; whereas the protomylonitic rock includes abundant epidote, titanite, chlorite, and sericite alteration of plagioclase. Quartz occurs as unoriented aggregates or weakly developed ribbons comprising anhedral grains ~50-500 µm long with irregular grain boundaries and variable subgrain development (Fig. 4G-J). Plagioclase occurs as porphyroclasts pervasively altered to sericite and mantled by epidote and biotite, defining a weak foliation (Fig. 4G,H). Epidote in protomylonites from Bowman's Wash are xenoblastic porphyroblasts and aggregates with abundant quartz inclusions (Figs. 4G-J, 5D-F), or xenoblastic vein filling. Both occurrences commonly contain high-REE allanite cores with sharp to diffuse boundaries (See Supplemental Material Fig. S3 and Fig. S4).

Based on mineral assemblages and microstructures, there is evidence for at least four petrogenetic generations of epidote (e.g., Fig. 4A-D): 1) magmatic epidote with REE-rich composition (allanite) partially recrystallized in the presence of fluids (cores of epidote porphryoclasts and porphyroblasts; Fig. 5); 2) low-REE metamorphic epidote crystallized at greenschist/lower amphibolite facies conditions (recrystallized rims of epidote porphryoclasts and porphyroblasts; Fig. 5); 3) epidote precipitated as veins from a fluid during brittle deformation (Fig. 4A-B); and finally, 4) minor epidote formed by saussuritization of plagioclase porphyroclasts in a few samples (Fig. 4C-D). Similar composition suggests that the recrystallized, low-REE rims of epidote porphyroclasts in the Cupcake Mountain Trail samples and porphyroblasts in the Bowman's Wash samples formed at a similar time and under similar fluid conditions.

$4.2 \, \delta^{18}O$ epidote and quartz data

Porphyroclastic and porphyroblastic epidote, recrystallized quartz and quartz inclusions within epidote are considered to be integral parts of the sample mylonitic fabrics and were analyzed for δ^{18} O by SIMS (See Fig. 5B). Epidote (and associated quartz) in other textural settings inferred to result from clearly late, lower-temperature, and/or fluid-mediated crystallization – e.g, vein and sausseritic epidote – were not analyzed to avoid the potential for isotope disequilibrium and erroneous thermometry results. SEM imaging of epidote porphyroclasts shows a variety of internal grain features that suggest chemical, and possibly isotopic, zonation (Fig. 5). The quartz-epidote pairs judged most likely to be in oxygen isotope equilibrium were either: (a) quartz inclusions paired with host epidote porphyroclast or porphyroblast; or (b) quartz ribbon in contact with epidote porphyroclast or porphyroblast.

Within epidote, SIMS analyses were sited within compositionally distinct, low-REE mantles and rims.

SIMS data show grain-to-grain oxygen isotope variations within both quartz and epidote (Fig. 7A), which generally decrease with distance from the main Whipple detachment surface. In the sample nearest to the fault ($Z_{det} < 1m$), quartz $\delta^{18}O$ values range from +7.2 to +9.9% and epidote $\delta^{18}O$ values range from +6.0 to -1.3% (Fig. 6A). At 6 m below the fault, quartz shows a very similar range of values from +7.8 to +10.0%, whereas the range in epidote $\delta^{18}O$ values decrease significantly to +6.1 to +3.9% (Fig. 6B). In the structurally deepest sample 40 m below the fault, quartz and epidote $\delta^{18}O$ values are tightly clustered, with quartz at +9.3 to +10.0% and epidote at +5.0 to +6.1% (Fig. 6C).

For Cupcake Mountain Trail samples, mean oxygen isotope fractionations ($\Delta^{18}O_{qz\text{-ep}}$) and variances generally increase with proximity to the WDF. Samples at Z_{det} = 40m, Z_{det} = 6m, and Z_{det} < 1m yield mean $\Delta^{18}O_{qz\text{-ep}}$ values and 2SD variances 3.96 ± 0.5, (n = 26 pairs), 3.65 ± 1.4 (n = 37 pairs), and 4.32 ± 4.5 (n = 42 pairs), respectively (Fig. 6; Tables S3-7). Fractionations between microstructurally linked mineral pairs at Z_{det} = 40m are tightly clustered in δ - δ plots (Fig. 6C) and become progressively more dispersed structurally upward at Z_{det} = 6m (Fig. 6B) and Z_{det} < 1m (Fig. 6A). At all structural levels, there are populations of mineral pairs at or near $\Delta^{18}O_{qz\text{-ep}}$ ~4‰ (Fig. 6D) In structurally shallower samples, dispersion spreads $\Delta^{18}O_{qz\text{-ep}}$ values across δ - δ isotherms and approximately parallel to the plot axes (Figs. 6A,B,D). Samples from Bowman's Wash at intermediate structural depths Z_{det} = 24 and Z_{det} = 26 m (WM-20-16 and WM-20-17) also show a range of $\Delta^{18}O_{qz\text{-ep}}$ values dispersed across δ - δ plot isotherms parallel to plot axes (Figs. S6 and Fig. S7).

We also examined mineral δ^{18} O ranges and fractionations as a function of quartz-epidote

pair microstructure. SIMS measurements targeted only inclusion-host pairs and matrixporphyroclast (Cupcake Mountain Trail) or matrix-porphyroblast (Bowman's Wash) pairs involving coarser-grained epidote and immediately adjacent quartz ribbons. In the deeper samples at $Z_{det} = 40 \text{m}$, $Z_{det} = 26 \text{m}$, and $Z_{det} = 24 \text{m}$, both inclusion and matrix quartz yield the same range of δ^{18} O values within analytical uncertainty for a given sample (see Supplemental Material Fig. S2E-S2F). Thus, within deeper samples, both microstructural types of quartzepidote pairs yield similar Δ^{18} O_{qz-ep} values, though pairs from Bowman's Wash involving epidote porphyroblasts give systematically larger $\Delta^{18}O_{qz-ep}$ than pairs from the Cupcake Mountain Trail involving epidote porphyroclasts (Supplemental Tables 3-7). In structurally shallower samples at $Z_{det} = 6m$ and $Z_{det} < 1m$, matrix quartz $\delta^{18}O$ extends to values $\sim 0.5\%$ lower than inclusion quartz δ^{18} O. Both microstructural types of quartz-epidote pairings at Z_{det} < 1m show large, bidirectional dispersion of Δ^{18} O_{qz-ep} along similar trends and over a similar range of Δ^{18} O_{qz-ep} values (Figs. 6A,D). At Z_{det} = 6m, both types of quartz-epidote pairs show significant unidirectional dispersion of Δ^{18} O_{qz-ep}, but inclusion-host pairs show a somewhat more limited dispersion than matrix-porphyroclast pairs (Fig. 6B,D). Overall, the similarities in δ^{18} O and Δ^{18} O_{qz-ep} between microstructural pair types at both sampling locations suggest that both inclusion and matrix quartz experienced variable isotopic resetting by a similar set of processes. The systematically larger fractionations in Bowman's Wash protomylonite suggest epidote porphyroblast crystallization occurred at different conditions (lower temperatures and/or higher fluid:rock ratio) than epidote porphyroclast recrystallization in the Cupcake Mountain Trail mylonite.

321

322

320

300

301

302

303

304

305

306

307

308

309

310

311

312

313

314

315

316

317

318

319

5. Discussion

In this discussion, we first compare the previous mineral separate $\delta^{18}O$ and SIMS-measured $\delta^{18}O$ records for the WDF footwall. We then detail the interpretative framework of the footwall refrigeration hypothesis, which invokes equilibrium oxygen isotope fractionation. This is followed by consideration of evidence that the fluid interacting within the footwall mylonite was a low- $\delta^{18}O$ meteoric fluid and that the interactions were occurring at mylonite-forming temperatures. We then analyze the patterns of oxygen isotope variation at different structural positions within the footwall and evaluate whether the patterns reflect a thermal gradient, as hypothesized for footwall refrigeration.

5.1 SIMS δ^{18} 0 versus bulk-mineral δ^{18} 0 data

SIMS can detect oxygen isotope variations at the spatial scale of micrometers and in textural context (e.g., Valley and Kita, 2009), permitting the scale of oxygen isotope exchange between and within individual minerals grains to be evaluated. The spatial resolution of mineral separate $\delta^{18}O$ data is effectively equivalent to the size of rock samples crushed for mineral separation. This lack of spatial resolution limits the analysis of data patterns beyond calculation of oxygen isotope fractionations as a function of structural depth. Intragrain SIMS $\delta^{18}O$ measurements allow for calculation of oxygen isotope fractionations as a function of structural depth and grain microstructure and also allow for inspection of trends in absolute mineral $\delta^{18}O$ values at each sampling depth.

As expected, SIMS-measured data show greater δ^{18} O variability in the Whipple footwall mylonites than was previously recognized through mineral separate data of Morrison and Anderson (1998) (Fig. 7). This is because SIMS directly samples (does not average) grain-scale and subgrain-scale domains that have experienced variable resetting of pre-deformation oxygen

isotope composition due to kinetic limitations (e.g., Bonamici et al., 2014; Eiler et al., 1993; Ferry et al., 2007; Page et al., 2023; Valley, 2001). The SIMS data closely reproduce the highest mineral δ^{18} O values of the mineral separate dataset but extend the previously recognized range of mineral δ^{18} O to lower values, including values as low as -1‰ for epidote (Fig. 7). In light of deformation and fluid-related microstructures detailed above (Figs. 4, 5), as well as comparison with equilibrium fractionation models (Fig. 8), we interpret the spread of mineral δ^{18} O from maximum values toward lower values as the record of heterogeneous, grain-scale fluid-rock exchange and variable isotopic resetting during mylonitization.

5.2 Predictions of equilibrium oxygen isotope fractionation: the interpretive framework of data underlying the footwall refrigeration hypothesis

The oxygen isotope compositions of minerals are a function of temperature and can also be a function of exchanging fluid composition (e.g., Nabelek, 1991; Baumgartner and Valley, 2001). In order to interpret the depth and fluid source of fluid-rock interactions from mineral δ^{18} O, both variables must be constrained. Thus, empirical and/or experimental calibrations of equilibrium oxygen isotope fractionations between quartz, epidote, and water (Fig. 8) provide a useful framework in which to analyze SIMS-measured mineral δ^{18} O values (Fig. 7). If the spatial scale of isotope analysis is larger than the spatial scale of isotope exchange, then fluid:rock ratio as a control on the extent of exchange must also be considered. SIMS can get around the need to constrain fluid:rock ratio because it is possible with careful textural analysis and deliberate targeting to analyze the range of fully exchanged to fully unexchanged mineral domains and determine isotope exchange mechanisms and vectors.

In the context of equilibrium fractionation, the footwall refrigeration model, which

assumes oxygen isotope equilibrium at the scale of the samples collected, predicts that quartz-epidote fractionations ($\Delta^{18}O_{qz\text{-ep}}$, distance between paired green and purple curves in Fig. 8) will increase upward, controlled by decreasing T toward the fluid-cooled detachment. If the interacting fluid composition was the same throughout the crustal column (a given blue line in Fig. 8), then equilibrium fractionation also predicts that individual mineral $\delta^{18}O$ values would increase upward toward the WDF in response to decreasing T (green or purple curves in Fig. 8). However, the footwall refrigeration model does not require a uniform fluid composition, and equilibrium fractionation (Fig. 8) predicts that for a given T at a specific depth, interactions with variable $\delta^{18}O$ water could produce potentially large dispersion in individual mineral $\delta^{18}O$ values. In particular, dispersion to lower mineral $\delta^{18}O$ is predicted during interactions with lower- $\delta^{18}O$ water. This will be discussed further below in section 5.4.

5.3 Evidence for the temperature range and fluid source of fluid-rock interactions in the Whipple footwall

The lowest δ^{18} O values measured in this study, -1‰ in epidote porphyroclast and porphyroblast rims, point to exchange with a low- δ^{18} O meteoric fluid at high temperature (Fig. 8). Epidote microstructures suggest dissolution-precipitation recrystallization (Fig. 5A), and it is reasonable to infer that this fluid-assisted recrystallization was also the mechanism of isotope exchange that produced the large range of SIMS-measured epidote δ^{18} O values. Assuming that epidote will not recrystallize outside of its thermodynamic phase stability range, the possible temperature for epidote-fluid isotope exchange is broadly bracketed by the lower stability limit of epidote at ~200°C (Bird and Spieler, 2004) and the upper thermometry constraints on Whipple mylonitization at 535-540 °C, as determined by feldspar solvus thermometry and Ti-in-quartz

thermometry (Anderson et al., 1988; Behr and Platt, 2011). Equilibrium fractionation models of epidote $\delta^{18}O$ as a function of water composition and temperature (Fig. 8) indicate that the lowest SIMS-measured epidote $\delta^{18}O$ values of -1% measured in this study required exchange with a fluid with $\delta^{18}O$ <0% for temperatures between 200-500°C (green curves in Fig. 8). In the region of the Whipple Mountains, modern meteoric water has $\delta^{18}O \approx$ -10% (Kendall and Coplen, 2001), and Miocene meteoric water has been reconstructed at $\delta^{18}O \approx$ -6% (Gébelin et al., 2012). The lowest SIMS-measured epidote $\delta^{18}O$ values could have been produced by exchange with meteoric fluid with $\delta^{18}O =$ -6%, if epidote recrystallized at the lowest-T end of its stability range. More likely, however, the low epidote $\delta^{18}O$ values reflect exchange at T > 200°C with a meteoric fluid already partially exchanged with a rock reservoir and thus somewhat higher in $\delta^{18}O$ than the original infiltrating meteoric water (i.e., -6% $< \delta^{18}O$ fluid < 0%).

Quartz $\delta^{18}O$ is dispersed to lower values over a more modest range (between ~10 and 7‰) than epidote $\delta^{18}O$ values. Quartz microstructures in the samples of this study record predominantly subgrain rotation recrystallization, which typically occurs at temperatures \geq 400 °C (Stipp et al., 2002). Assuming oxygen isotope exchange between quartz and fluid during subgrain rotation recrystallization down to 400 °C, the lowest quartz $\delta^{18}O$ values at 7‰ indicate an exchanging fluid $\delta^{18}O$ of 3‰, consistent with a low- $\delta^{18}O$ fluid partially exchanged with a rock reservoir. If more limited and/or localized crystal-plastic recrystallization of quartz continued down to 300 °C (e.g., Hirth and Tullis, 1992), then quartz $\delta^{18}O = 7\%$ indicates an exchanging fluid $\delta^{18}O$ of 0‰. The generally higher fluid $\delta^{18}O$ values inferred from quartz as compared to epidote suggests that the $\delta^{18}O$ of infiltrating fluid varied over time, even at a given structural depth, and that the temperatures and times over which these two minerals recrystallized may have overlapped but were not identical.

416

417

418

419

420

421

422

423

424

425

426

427

428

429

430

431

432

433

434

435

436

437

5.4 Thermal gradient vs. fluid-interaction gradient

In this section, we focus on the three samples collected from the Cupcake Mountain Trail locale (Fig. 2) because these define a depth transect from Z_{det} <1m to Z_{det} = 40m through the same lithology. The two samples from the Bowman's Wash locale are closely spaced and provide little leverage on the depth variation in oxygen isotope trends, although they provide a more direct comparison with the results of Morrison and Anderson (1998) (Supplemental Materials).

The sample farthest below the WDF along the Cupcake Mountain Trail Traverse ($Z_{det} =$ 40m) provides a reference point for comparison of structurally shallower samples because it was presumably the hottest and the least affected by meteoric fluid interactions. This deep sample shows relatively tight clustering of mineral δ^{18} O values (~9.5-10% in quartz and ~5.5-6% in epidote) and $\Delta^{18}O_{qz-ep}$ pair values (Figs. 6D, 7A) suggests that the measured $\Delta^{18}O_{qz-ep}$ gradient does not reflect a temperature gradient. In samples with Z_{det} < 40 m, SIMS measurements reveal maximum mineral δ^{18} O values similar to the Z_{det} = 40m reference sample (~9.5-10‰ in quartz and ~5.5-6\% in epidote) and dispersion toward lower values, opposite the direction of Tcontrolled δ^{18} O variation predicted by equilibrium fractionation (Fig. 8). However, as noted above in section 5.2, equilibrium fractionation modeling suggests the possibility of large mineral δ^{18} O dispersion with fluid-rock interactions involving variable- δ^{18} O fluids (Fig. 8). Taking the averages of dispersed SIMS-measured mineral δ^{18} O values at each structural depth produces an apparent increase in the Δ^{18} O_{qz-ep} approaching the WDF (Fig. 6D) because epidote shows greater δ^{18} O dispersion than quartz (Fig. 7A). We suggest that this upward apparent increase in Δ^{18} O_{qz-ep} is effectively what Morrison and Anderson (1998) measured with mineral separate data and then interpreted to reflect a paleo-thermal gradient.

The dispersion patterns of $\Delta^{18}O_{qz\text{-ep}}$ pairs (Fig. 6) also suggest that quartz and epidote exchanged oxygen isotopes differentially with the meteoric fluid. If quartz and epidote $\delta^{18}O$ were lowered via the same fluid-rock interaction mechanism, then their $\delta^{18}O$ values should show sloped, covarying trends on δ - δ plots, and $\Delta^{18}O_{qz\text{-ep}}$ values should maintain single-peaked, centralized distributions, though broader and shifted, in kernel density plots. Instead, the axis-parallel linear data trends on δ - δ plots (Figs. 6B,C) and multi-peaked distributions in KDE plots (Fig. 6D) indicate independent variation in quartz and epidote $\delta^{18}O$ values. Based on microstructural observations, quartz-fluid exchange occurred primarily during subgrain rotation recrystallization (c.f., Quilichini et al., 2015; Siebenaller et al., 2016). In contrast, epidote-fluid exchange occurred primarily through dissolution-precipitation recrystallization (Fig. 5). These inferred exchange mechanisms were likely active over different timescales, different T ranges, and variable fluid compositions (see section 5.3). Thus, our data suggest that meteoric fluid-rock interaction likely occurred over a range of temperatures within the same rock volume.

Nonetheless, SIMS data also suggest that meteoric fluid-rock interactions were spatially heterogeneous at the scale of grains to mm-scale domains, resulting in local preservation of metamorphic quartz-epidote oxygen isotope equilibrium unaffected by infiltrating meteoric fluid. These preserved domains should reflect solely T-controlled equilibrium oxygen isotope fractionation and retain a record of the footwall temperature at each sampled depth. Considering microstructurally linked quartz-epidote pairs measured by SIMS along the Cupcake Mountain Trail traverse (samples at Zdet = 1m, 6m, and 40m in Fig. 6), the highest SIMS-measured δ^{18} O values and the fractionations between these maximum values (Δ^{18} O_{qz-ep} = 4.0 ± 0.4‰) are nearly the same at all sampled structural depths (Tables S3-5; Fig. 6). In other words, the local sample

domains that preserve T-controlled isotopic equilibrium record the same $\Delta^{18}O_{qz\text{-ep}}$ and therefore the same temperature over the whole depth transect. Using the calibration of Matthews (1994), this suggests an essentially uniform temperature of 521 +43/-37°C from the fault to a structural depth of 40 m, yielding no detectable paleo-thermal gradient in the upper 40 m of the footwall beneath the WDF.

In summary, SIMS in situ oxygen isotope data suggest that most of the $\Delta^{18}O_{qz\text{-ep}}$ values determined in mineral separates by Morrison and Anderson (1998) were averages of dispersed, disequilibrium fractionations and were not appropriate for oxygen isotope thermometry or assessment of the footwall paleo-thermal gradient. Instead, our data show that the dominant $\delta^{18}O$ signature in the Whipple footwall mylonites below the WDF is the result of fluid interactions. Careful analysis of SIMS data patterns also identifies rock domains that preserve oxygen isotopes values and fractionations unaffected by meteoric fluid interactions, and these show no evidence for a thermal gradient. Therefore, this study finds evidence for spatially and temporally variable fluid interactions at midcrustal depths but no evidence for footwall refrigeration.

6. Conclusions

Interpretation of oxygen isotope records in metamorphic core complexes is a long-standing challenge because of the competing effects of fluid composition, temperature, and fluid:rock mass balance on final rock and mineral oxygen isotope compositions (e.g. Gébelin et al., 2015; Gottardi et al., 2013; Quilichini et al., 2016; Scott et al., 1998; Smith et al., 1991; Wickham et al., 1993). In this study, in situ δ^{18} O measurements by SIMS aide in distinguishing the effects of temperature versus fluids in the δ^{18} O record of core complex mylonites for the first time. SIMS reveals changes in δ^{18} O with depth in the Whipple MCC footwall that record

increasing fluid-rock interactions toward the main detachment fault surface. In situ $\delta^{18}O$ measurements targeting specific quartz and epidote zones and microstructures show greater oxygen isotope variability in Whipple footwall rocks than previously detected. Low absolute epidote $\delta^{18}O$ values require high-T interactions with a meteoric, low- $\delta^{18}O$ fluids. Thus, low $\delta^{18}O$ in Whipple mylonites represents an unequivocal *oxygen isotope* record of meteoric fluid infiltration to midcrustal depths synchronous with extensional deformation and active mylonite development.

Nonetheless, while many quartz and epidote $\delta^{18}O$ values have been partially reset by meteoric fluid-rock oxygen isotope exchange, microstructural context and in situ SIMS analysis identifies a subset of $\delta^{18}O$ values in all samples that preserve equilibrium (metamorphic) isotope fractionations. These fractionations record high T equilibrium (>500°C) and reveal little or no T variation in the upper 40 m of the Whipple detachment footwall. We therefore conclude that there is no oxygen isotope evidence of spatial variation in crustal thermal structure around the WDF and therefore no indication of a large paleo-thermal gradient that suggests footwall refrigeration.

Finally, SIMS data showing grain-scale spatial heterogeneity of meteoric fluid interactions provide little support for high meteoric fluid:rock ratios along the WDF as implied by the footwall refrigeration hypothesis. Consequently, we consider it unlikely that 1) meteoric water infiltration alone could have generated high pore-fluid pressures along the WDF, or that, 2) advective heat removal by cool meteoric fluids could have been efficient enough to perturb thermochronometers in the footwall prior to footwall exhumation.

Acknowledgements

508

509

510

511

512

513

514

515

507

This work was funded through NSF award 1650355 to Dr. Chloë Bonamici, the EAR award 2004618 to the WiscSIMS facility, and the UW-Madison Geoscience Department Bailey Fellowship to Claudia I. Roig González. Dr. Adrian Castro assisted with fieldwork. Drae Rogers provided expert sample preparation. Mike Spicuzza provided training in sample preparation and assisted with oxygen isotope standard development. Bil Schneider provided expert assistance with imaging by proxy during COVID-19 lockdown and in-person afterwards. We thank Raphaël Gottardi and an anonymous reviewer for pushing this work toward greater clarity.

516

517

518

519

520

523

References

- Anderson, J.L., Barth, A.P., Young, E.D., 1988. Mid-crustal Cretaceous roots of Cordilleran metamorphic core complexes. Geology 16, 366–369. https://doi.org/10.1130/0091-7613(1988)016<0366:MCCROC>2.3.CO;2.
- Anderson, J.L., Cullers, R.L., 1990. Chapter 4: Middle to upper crustal plutonic construction of a 521 magmatic arc; An example from the Whipple Mountains metamorphic core complex, in: 522 Anderson, J.L. (Ed.), The Nature and Origin of Cordilleran Magmatism. Geological Society
- of America, p. 0. https://doi.org/10.1130/MEM174-p47. 524
- 525 Axen, G.J., 1992. Pore pressure, stress increase, and fault weakening in low-angle normal
- 526 faulting. J. Geophys. Res.: Solid Earth 97, 8979–8991. https://doi.org/10.1029/92JB00517.
- 527 Axen, G.J., Selverstone, J., 1994. Stress state and fluid-pressure level along the Whipple
- 528 detachment fault, California. Geology 22, 835-838. https://doi.org/10.1130/0091-
- 529 7613(1994)022<0835:SSAFPL>2.3.CO;2.

- Behr, W.M., Platt, J.P., 2011. A naturally constrained stress profile through the middle crust in
- an extensional terrane. Earth Planet. Sci. Lett. 303, 181–192.
- https://doi.org/10.1016/j.epsl.2010.11.044.
- Beratan, K.K., 1991. Miocene Synextension Sedimentation Patterns, Whipple Mountains,
- Southeastern California' Implications for the Geometry of the Whipple Detachment System.
- J. Geophys. Res. 96, 425–442.
- Bird, D., Spieler, A.R., 2004. Epidote in Geothermal Systems. Rev. Mineral. Geochemistry. 56,
- 537 235-300.
- Block, L., Royden, L.H., 1990. Core complex geometries and regional scale flow in the lower
- crust. Tectonics 9, 557–567. https://doi.org/10.1029/TC009i004p00557.
- Bonamici, C.E., Kozdon, R., Ushikubo, T., Valley, J.W., 2014. Intragrain oxygen isotope zoning
- in titanite by SIMS: Cooling rates and fluid infiltration along the Carthage-Colton Mylonite
- Zone, Adirondack Mountains, NY, USA. J. Metamorph. Geol. 32, 71–92.
- 543 https://doi.org/10.1111/jmg.12059.
- Coney, P.J., 1980. Cordilleran metamorphic core complexes: An overview. Mem. Geol. Soc.
- 545 Am. 153, 7–31. https://doi.org/10.1130/MEM153-p7.
- Davis, G.A., 1988. Rapid upward transport of mid-crustal mylonitic gneisses in the footwall of a
- Miocene detachment fault, Whipple Mountains, southeastern California. Geol. Rundschau
- 77, 191–209. https://doi.org/10.1007/BF01848684.
- Davis, G. A., and Anderson, J. L., 1991. Low angle normal faulting and rapid uplift of mid-
- crustal rocks in the Whipple Mountains metamorphic core complex, southeastern
- California: discussion and field guide. In: Geological Excursions in Southern California and
- Mexico (Ed. by M. J. Walawender and B. B. Hanan). Guidebook for Geological Society of

- America 1991 Annual Meeting, Department of Geological Sciences, San Diego State
- University, San Diego, California, 417–446.
- Davis, G.A., Anderson, J.L., Frost, E.G., Shackelford, T.J., 1980. Mylonitization and detachment
- faulting in the Whipple-Buckskin-Rawhide Mountains terrane, southeastern California and
- western Arizona. Mem. Geol. Soc. Am. 153, 79–129. https://doi.org/10.1130/MEM153-
- 558 p79.
- Davis, G.A., Lister, G.S., Reynolds, S.J., 1986. Structural evolution of the Whipple and South
- mountains shear zones, southwestern United States. Geology 14, 7–10.
- 561 https://doi.org/10.1130/0091-7613(1986)14<7:SEOTWA>2.0.CO;2.
- Dessimoz, M., 2011. Epidote in hydrous mafic magmas: near solidus phase relations in the lower
- crust (M.S.). Université de Lausanne, Faculté des géosciences et de l'environnement.
- Dorsey, R.J., Becker, U., 1995. Evolution of a large miocene growth structure in the upper plate
- of the Whipple detachment fault, Northeastern Whipple Mountains, California. Basin Res.
- 7, 151–163. https://doi.org/10.1111/j.1365-2117.1995.tb00101.x.
- Dusséaux, C., Gébelin, A., Boulvais, P., Gardien, V., Grimes, S., Mulch, A., 2019. Meteoric
- fluid-rock interaction in Variscan shear zones. Terra Nova 31, 366–72.
- Eiler, J.M., Valley, J.W., Baumgartner, L.P., 1993. A new look at stable isotope thermometry.
- Geochim. Cosmochim. Acta. 57, 2571-2583. https://doi.org/10.1016/0016-
- 571 7037(93)90418-V.
- Ferry, J.M., Watson, E.B., 2007. New thermodynamic models and revised calibrations for the Ti-
- in-zircon and Zr-in-rutile thermometers. Contrib. Mineral. Petrol. 154, 429–437.
- 574 https://doi.org/10.1007/s00410-007-0201-0.
- 575 Fricke, H.C., Wickham, S.M., O'Neil, J.R., 1992. Oxygen and hydrogen isotope evidence for

- meteoric water infiltration during mylonitization and uplift in the Ruby Mountains-East
- Humboldt Range core complex, Nevada. Contrib. to Mineral. Petrol. 111, 203–221.
- 578 https://doi.org/10.1007/BF00348952.
- Gans, P.B., Gentry, B.J., 2016. Dike emplacement, footwall rotation, and the transition from
- magmatic to tectonic extension in the Whipple Mountains metamorphic core complex,
- southeastern California. Tectonics 35, 2564–2608. https://doi.org/10.1002/2016TC004215.
- 582 Gébelin, A., Mulch, A., Teyssier, C., Heizler, M., Vennemann, T., Seaton, N.C.A., 2011. Oligo-
- Miocene extensional tectonics and fluid flow across the Northern Snake Range detachment
- system, Nevada. Tectonics 30, 1–18. https://doi.org/10.1029/2010TC002797.
- Gébelin, A., Mulch, A., Teyssier, C., Page Chamberlain, C., Heizler, M., 2012. Coupled basin-
- detachment systems as paleoaltimetry archives of the western North American Cordillera.
- Earth Planet. Sci. Lett. 335–336, 36–47. https://doi.org/10.1016/j.epsl.2012.04.029.
- Gébelin, A., Teyssier, C., Heizler, M.T., Mulch, A., 2015. Meteoric water circulation in a
- rolling-hinge detachment system (northern snake range core complex, Nevada). Bull. Geol.
- 590 Soc. Am. 127, 149–161. https://doi.org/10.1130/B31063.1.
- 591 Gottardi, R., Teyssier, C., Mulch, A., Vennemann, T.W., Wells, M.L., 2011. Preservation of an
- extreme transient geotherm in the Raft River detachment shear zone. Geology 39, 759–762.
- 593 https://doi.org/10.1130/G31834.1.
- Gottardi, R., and Teyssier, C., 2013. Thermomechanics of an extensional shear zone, Raft River
- metamorphic core complex, NW Utah. J. Struct. Geol. 53, 54-69.
- 596 https://doi.org/10.1016/j.jsg.2013.05.012.
- 597 Gottardi, R., Kao, P.-H., Saar, M.O., Teyssier, C., 2013. Effects of permeability fields on fluid,
- heat, and oxygen isotope transport in extensional detachment systems: Effects of

- permeability fields. Geochem. Geophys. Geosyst. 14, 1493–1522.
- 600 https://doi.org/10.1002/ggge.20100.
- 601 Gottardi, R., Teyssier, C., Mulch, A., Valley, J.W., Spicuzza, M.J., Vennemann, T.W.,
- Quilichini, A., Heizler, M., 2015. Strain and permeability gradients traced by stable isotope
- exchange in the Raft River detachment shear zone, Utah. J. Struct. Geol. 71, 41–57.
- 604 https://doi.org/10.1016/j.jsg.2014.10.005.
- 605 Gottardi, R., Schaper, M.C., Barnes, J.D., Heizler, M.T., 2018. Fluid–Rock Interaction and Strain
- Localization in the Picacho Mountains Detachment Shear Zone, Arizona, USA. Tectonics
- 607 37, 3244–3260. https://doi.org/10.1029/2017TC004835.
- Gregory, R.T., and Taylor, H.P., 1981. An Oxygen Isotope in a Section of Cretaceous Oceanic
- 609 Crust, Samail Ophiolite, Oman: Evidence for δ^{18} O Buffering of the Oceans by Deep (>5
- 610 km) Seawater-Hydrothermal Circulation at Mid-Ocean Ridges. J. Geophys. Res. 86, 2737–
- 611 2755. https://doi.org/10.1029/JB086iB04p02737.
- Hacker, B.R., Yin, A., Christie, J.M., Davis, G.A., 1992. Stress magnitude, strain rate, and
- 613 rheology of extended Middle Continental Crust inferred from quartz grain sizes in the
- Whipple Mountains, California. Tectonics 11, 36–46. https://doi.org/10.1029/91TC01291.
- Haines, S., Lynch, E., Mulch, A., Valley, J.W., van der Pluijm, B., 2016. Meteoric fluid
- infiltration in crustal-scale normal fault systems as indicated by δ^{18} O and δ^{2} H geochemistry
- and 40Ar/39Ar dating of neoformed clays in brittle fault rocks. Lithosphere 8, 587–600.
- 618 https://doi.org/10.1130/L483.1.
- 619 Hirth, G., & Tullis, J. A. N. (1992). Dislocation creep regimes in quartz aggregates. Journal of
- 620 Structural Geology, 14(2), 145-159.
- Kelly, J.L., Fu, B., Kita, N.T., Valley, J.W., 2007. Optically continuous silcrete quartz cements

- of the St. Peter Sandstone: High precision oxygen isotope analysis by ion microprobe.
- Geochim. Cosmochim. Acta. 71, 3812–3832. https://doi.org/10.1016/j.gca.2007.05.014.
- Kendall, C., and Coplen, T., 2001. Distribution of oxygen-18 and deuterium in river waters
- across the United States. Hydrol. Process. 15, 1363–1393. https://doi.org/10.1002/hyp.217.
- Kita, N.T., Ushikubo, T., Fu, B., Valley, J.W., 2009. High precision SIMS oxygen isotope
- analysis and the effect of sample topography. Chem. Geol. 264, 43–57.
- https://doi.org/10.1016/j.chemgeo.2009.02.012.
- Kronenberg, A. K., 1994. Hydrogen speciation and chemical weakening of quartz. Rev. Mineral.
- Geochemistry, 29, 123-176. DOI: 10.2138/rmg.1994.29.4.
- Kohlstedt, D.L., 2006. The role of water in high-temperature rock deformation. Rev. Mineral.
- Geochemistry 62, 377–396. https://doi.org/10.2138/rmg.2006.62.16.
- Linzmeier, B. J., Kitajima, K., Denny, A. C., and Cammack, J. N., 2018. Making maps on a
- 634 micrometer scale. Eos, 99. https://doi.org/10.1029/2018EO099269.
- Lister, G.S., Davis, G.A., 1989. The origin of metamorphic core complexes and detachment
- faults formed during Tertiary continental margins. J. Struct. Geol. 11, 65–94.
- 637 https://doi.org/10.1016/0191-8141(89)90036-9.
- Losh, S., 1997. Stable isotope and modeling studies of fluid-rock interaction associated with the
- Snake Range and Mormon Peak detachment faults, Nevada. Bull. Geol. Soc. Am. 109, 300–
- 323. https://doi.org/10.1130/0016-7606(1997)109<0300:SIAMSO>2.3.CO;2.
- Matthews, A., 1994. Oxygen isotope geothermometers for metamorphic rocks. J. Metamorph.
- Geol. 12, 211–219. https://doi.org/10.1111/j.1525-1314.1994.tb00017.x.
- Matsuhisa, Y., Goldsmith, J.R., Clayton, R.N., 1979. Oxygen isotopic fractionation in the system
- quartz-albite-anorthite-water. Geochim. Cosmochim. Acta. 43, 1131-1140.

- https://doi.org/10.1016/0016-7037(79)90099-1.
- McCaig, A.M., 1989. Fluid flow through fault zones. Nature 340, 600.
- 647 https://doi.org/10.1038/340600a0.
- McCaig, A.M., Wickham, S.M., Taylor, H.P., 1990. Deep fluid circulation in alpine shear zones,
- Pyrenees, France: field and oxygen isotope studies. Contrib. Mineral. Petrol. 106, 41–60.
- https://doi.org/10.1007/BF00306407.
- McFadden, R.R., Mulch, A., Teyssier, C., Heizler, M., 2015. Eocene extension and meteoric
- fluid flow in the Wildhorse detachment, Pioneer metamorphic core complex, Idaho.
- Lithosphere 7, 355–366. https://doi.org/10.1130/1429.1.
- Methner, K., Mulch, A., Teyssier, C., Wells, M.L., Cosca, M.A., Gottardi, R., Gébelin, A.,
- Chamberlain, C.P., 2015. Eocene and Miocene extension, meteoric fluid infiltration, and
- core complex formation in the Great Basin (Raft River Mountains, Utah). Tectonics 34,
- 657 680–693. https://doi.org/10.1002/2014TC003766.
- Morrison, J., 1994. Meteoric water-rock interaction in the lower plate of the Whipple Mountain
- metamorphic core complex, California. J. Metamorph. Geol. 12, 827-840.
- https://doi.org/10.1111/j.1525-1314.1994.tb00062.x.
- Morrison, J., Anderson, J.L., 1998. Footwall refrigeration along a detachment fault: Implications
- for the thermal evolution of core complexes. Science 279, 63–66.
- https://doi.org/10.1126/science.279.5347.63.
- Page, F.Z., Storey, C.D., 2023. A rutile and titanite record of subduction fluids: Integrated
- oxygen isotope and trace element analyses in Franciscan high-pressure rocks. J.
- Metamorph. Geol. 1–20. https://doi.org/10.1111/jmg.12717.
- Person, M., Mulch, A., Teyssier, C., Gao, Y., 2007. Isotope transport and exchange within

- metamorphic core complexes. Am. J. Sci. 307, 555–589.
- https://doi.org/10.2475/03.2007.01.
- Platt, J.P., Behr, W.M., Cooper, F.J., 2015. Metamorphic core complexes: windows into the
- mechanics and rheology of the crust. J. Geol. Soc. London. 172, 9–27.
- https://doi.org/10.1144/jgs2014-036.
- Quilichini, A., Siebenaller, L., Nachlas, W.O., Teyssier, C., Vennemann, T.W., Heizler, M.T.,
- Mulch, A., 2015. Infiltration of meteoric fluids in an extensional detachment shear zone
- 675 (Kettle dome, WA, USA): How quartz dynamic recrystallization relates to fluid-rock
- interaction. J. Struct. Geol., 71, 71–85. https://doi.org/10.1016/j.jsg.2014.11.008.
- Quilichini, A., Siebenaller, L., Teyssier, C., Vennemann, T.W., 2016. Magmatic and meteoric
- fluid flow in the Bitterroot extensional detachment shear zone (MT, USA) from ductile to
- brittle conditions. J. Geodyn. 101, 109–128. https://doi.org/10.1016/j.jog.2016.05.006.
- Quinn, R.J., Kitajima, K., Nakashima, D., Spicuzza, M.J., Valley, J.W., 2017. Oxygen isotope
- thermometry using quartz inclusions in garnet. J. Metamorph. Geol. 35, 231–252.
- 682 https://doi.org/10.1111/jmg.12230.
- Roig González, C.I., Bonamici, C., Blum, T., Nachlas, W.O., Spicuzza, M., 2023. Epidote
- Reference Material Development Calibrated for Oxygen Isotope Determination by
- Secondary Ion Mass Spectrometry (SIMS). Microsc. Microanal. 29, 221–222.
- https://doi.org/10.1093/micmic/ozad067.098.
- Scott, R.J., Foster, D.A., Lister, G.S., 1998. Tectonic implications of rapid cooling of lower plate
- rocks from the Buckskin-Rawhide metamorphic core complex, west-central Arizona. Bull.
- Geol. Soc. Am. 110, 588–614. https://doi.org/10.1130/0016-
- 690 7606(1998)110<0588:TIORCO>2.3.CO;2.

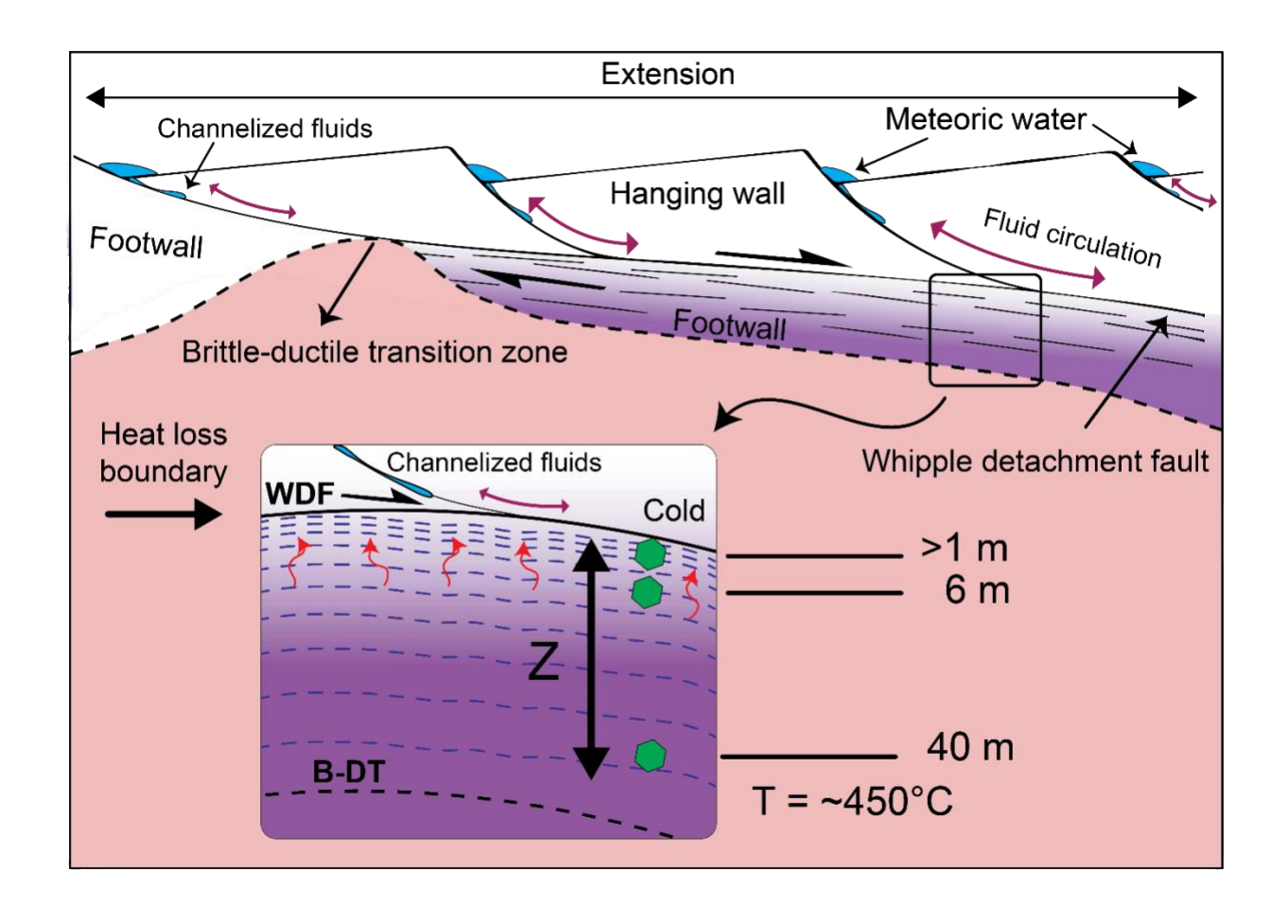
- 691 Selverstone, J., Axen, G.J., Luther, A., 2012. Fault localization controlled by fluid infiltration
- into mylonites: Formation and strength of low-angle normal faults in the midcrustal brittle-
- plastic transition. J. Geophys. Res. Solid Earth 117. https://doi.org/10.1029/2012JB009171.
- 694 Sibson, R.H., 2000. Fluid involvement in normal faulting. J. Geodyn. 29, 469–499.
- 695 https://doi.org/10.1016/S0264-3707(99)00042-3.
- 696 Siebenaller, L., Vanderhaeghe, O., Jessell, M., Boiron, M.C., Hibsch, C., 2016. Syntectonic
- fluids redistribution and circulation coupled to quartz recrystallization in the ductile crust
- 698 (Naxos Island, Cyclades, Greece). J. Geodyn. 101, 129–41.
- 699 https://doi.org/10.1016/j.jog.2016.07.001.
- Singleton, J.S., Mosher, S., 2012. Mylonitization in the lower plate of the Buckskin-Rawhide
- detachment fault, west-central Arizona: Implications for the geometric evolution of
- metamorphic core complexes. J. Struct. Geol. 39, 180–198.
- 703 https://doi.org/10.1016/j.jsg.2012.02.013.
- Singleton, J.S., Stockli, D.F., Gans, P.B., Prior, M.G., 2014. Timing, rate, and magnitude of slip
- on the Buckskin-Rawhide detachment fault, west central Arizona. Tectonics 33, 1596–1615.
- 706 https://doi.org/10.1002/2013TC003517.
- Smith, B.M., Reynolds, S.J., Day, H.W., Bodnar, R.J., 1991. Deep-seated fluid involvement in
- ductile-brittle deformation and mineralization, South Mountains metamorphic core
- 709 complex, Arizona. Bull. Geol. Soc. Am. 103, 559–569. https://doi.org/10.1130/0016-
- 710 7606(1991)103<0559:DSFIID>2.3.CO;2.
- Spencer, J.E., Reynolds, S.J., 1990. Relationship between Mesozoic and Cenozoic Tectonic
- features in west central Arizona and adjacent southeastern California. J. Geophys. Res. 95,
- 713 539–555. https://doi.org/10.1029/JB095iB01p00539.

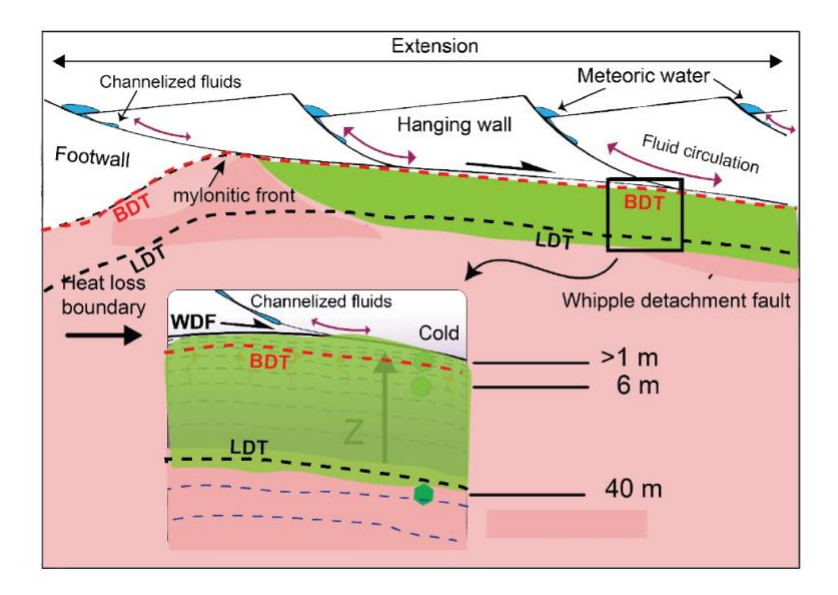
- Stockli, D.F., Brichau, S., Dewane, T.J., Hager, C., Schroeder, J., 2006. Dynamics of large-
- magnitude extension in the Whipple Mountains metamorphic core complex. Geochimica et
- 716 Cosmochimica Acta 70, A616. https://doi.org/10.1016/j.gca.2006.06.1143.
- 717 Tirel, C., Brun, J.P., Burov, E., 2008. Dynamics and structural development of metamorphic core
- 718 complexes. J. Geophys. Res. Solid Earth 113, 1–25. https://doi.org/10.1029/2005JB003694.
- Valley, J.W., 2001. Stable isotope thermometry at high temperatures. Rev. Mineral.
- Geochemistry. 43, 365–402. https://doi.org/10.2138/gsrmg.43.1.365.
- Wang, X. L., Coble, M.A., Valley, J.W., Shu, X. J., Kitajima, K., Spicuzza, M.J., Sun, T., 2014.
- Influence of radiation damage on Late Jurassic zircon from southern China: Evidence from
- in situ measurements of oxygen isotopes, laser Raman, U–Pb ages, and trace elements.
- 724 Chem. Geol. 389, 122–136. https://doi.org/10.1016/j.chemgeo.2014.09.013.
- Whitney, D.L., Teyssier, C., Rey, P., Roger Buck, W., 2013. Continental and oceanic core
- complexes. Bull. Geol. Soc. Am. 125, 273–298. https://doi.org/10.1130/B30754.1.
- Wickham, S.M., Peters, M.T., Fricke, H.C., O'Neil, J.R., 1993. Identification of magmatic and
- meteoric fluid sources and upward- and downward-moving infiltration fronts in a
- metamorphic core complex. Geology 21, 81–84. https://doi.org/10.1130/0091-
- 730 7613(1993)021<0081:IOMAMF>2.3.CO;2.
- Wooden, J.L., Wright, J.E., Howard, K., Barth, A.P., Anderson, J.L., 2017. Implications of new
- 732 SIMS zircon ages for magmatic evolution of the Whipple Mountains metamorphic core
- complex, in: Geological Society of America Abstracts with Programs. Presented at the
- GSA Annual Meeting, Seattle, Washington, USA.
- 735 <u>https://doi.org/10.1130/abs/2017AM-299472</u>
- Wright, J.E., Anderson, J.L., Davis, G.A., 1986. Timing of plutonism, mylonitization, and

737	decompression in a metamorphic core complex, Whipple Mountains, California, in:
738	Geological Society of America Abstracts with Programs. p. 201.
739	Yin, A., Dunn, J.F., 1992. Structural and stratigraphic development of the Whipple-Chemehuevi
740	detachment fault system, southeastern California: implications for the geometrical evolution
741	of domal and basinal low-angle normal faults. Geol. Soc. Am. Bull. 104, 659-674.
742	https://doi.org/10.1130/0016-7606(1992)104<0659:SASDOT>2.3.CO;2.
743	Zheng, Y. F., 1993a. Calculation of oxygen isotope fractionation in hydroxyl-bearing silicates.

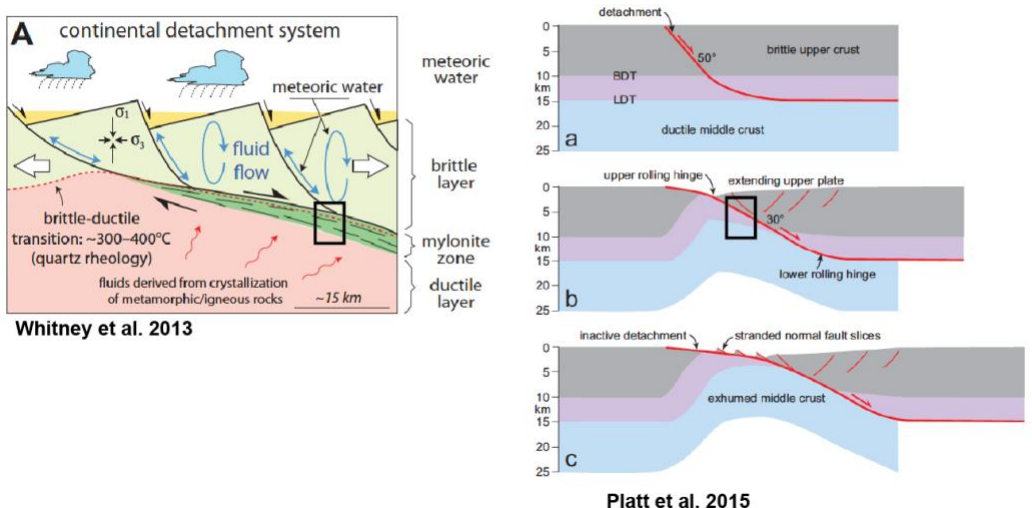
Earth Planet. Sci. Lett. 121, 247–263. https://doi.org/10.1016/0012-821X(93)90243-3.

744





- 1) make sure BDT and LDT are correctly located and labeled (Whitney and Platt figs below for our reference)
- 2) BDT and LDT should be parallel to isotherms in the inset figure
- 3) Let's just remove the temperature from this figure to avoid confusion.
- 4) change purple to green (like Whitney) and remove the color gradient (it is confusing because of the isotherms)



al. **2015** Figure 1:

Schematic diagram of a detachment fault system in a continental metamorphic core complex (modified from Whitney et al.(2013) and Platt et al. (2015)). Inset expands the footwall region below the main detachment fault surface and schematically shows how, in the footwall refrigeration hypothesis, circulation of cool meteoric fluids along the detachment effectively shifts the major heat loss boundary from Earth's surface downward to the detachment fault surface with the result that crustal isotherms (blue dashed lines) are compressed beneath the detachment. Footwall mylonites between the brittle-ductile transition (BDT) and localized-distributed deformation transition (LDT) are exhumed toward the WDF. The BDT occurs at ~300°C, whereas the LDT occurs at ~500°C (Platt et al., 2015). Green shading shows footwall region variably affected by meteoric fluid infiltration. Purple polygons schematically indicate

sample depths below the detachment that were investigated in this study for quartz-epidote oxygen isotope fractionation and thermometry. ...

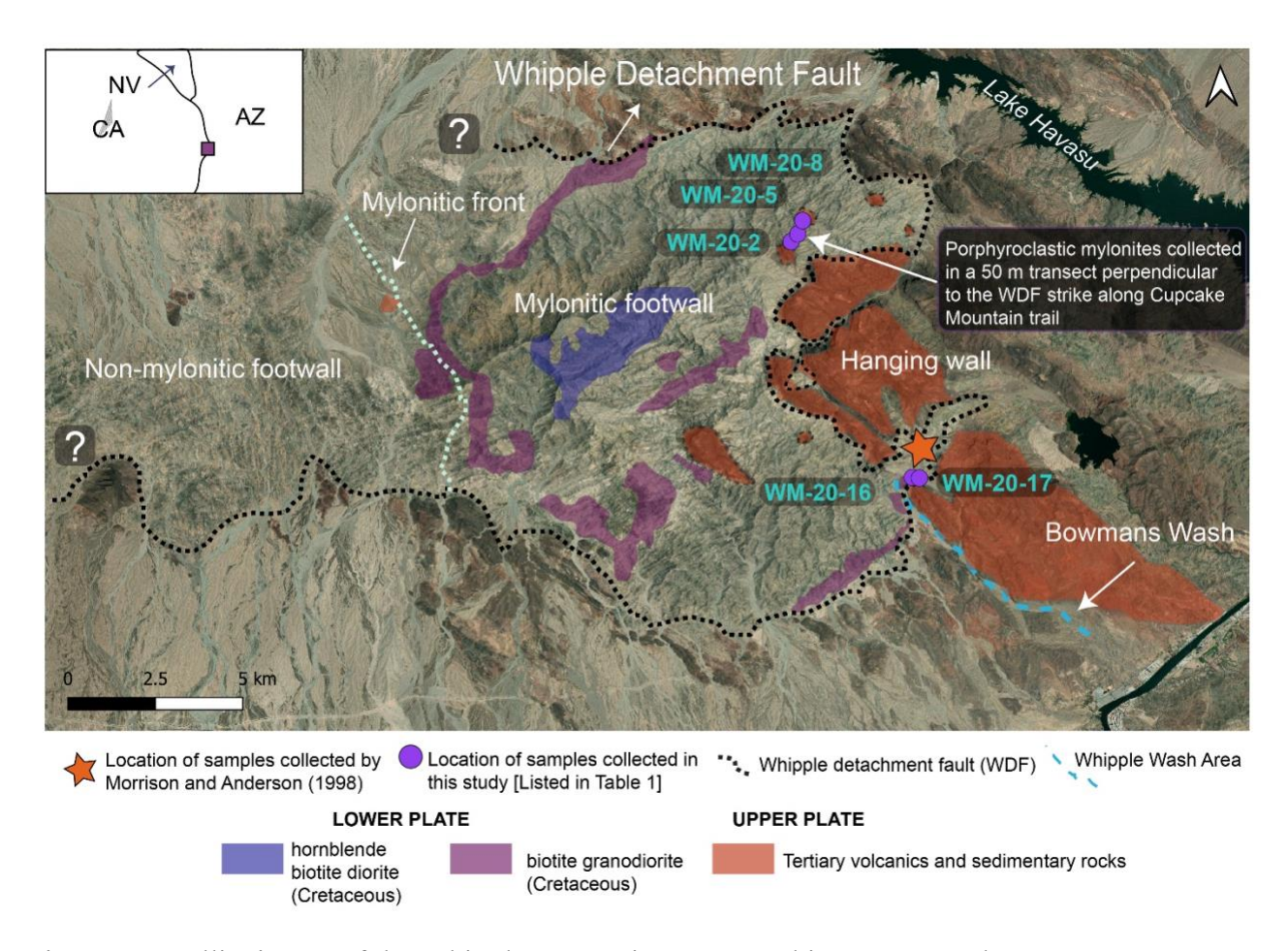


Figure 2: Satellite image of the Whipple Mountain Metamorphic Core Complex. Inset schematically shows location of the Whipple Mountain MCC on the Arizona (AZ)-California (CA)-Nevada (NV) border region with the study area indicated by the purple square. Purple circles indicate where samples for this field campaign were collected. Blue font are the n=5 samples in this study. Black dashed line is a projection of the Whipple Detachment Fault (WDF) on the detachment surface. Orange star is the Bowman's Wash locality sampled by Morrison and Anderson (1998). Unit overlays of hanging wall and footwall rocks are after Behr and Platt (2011).

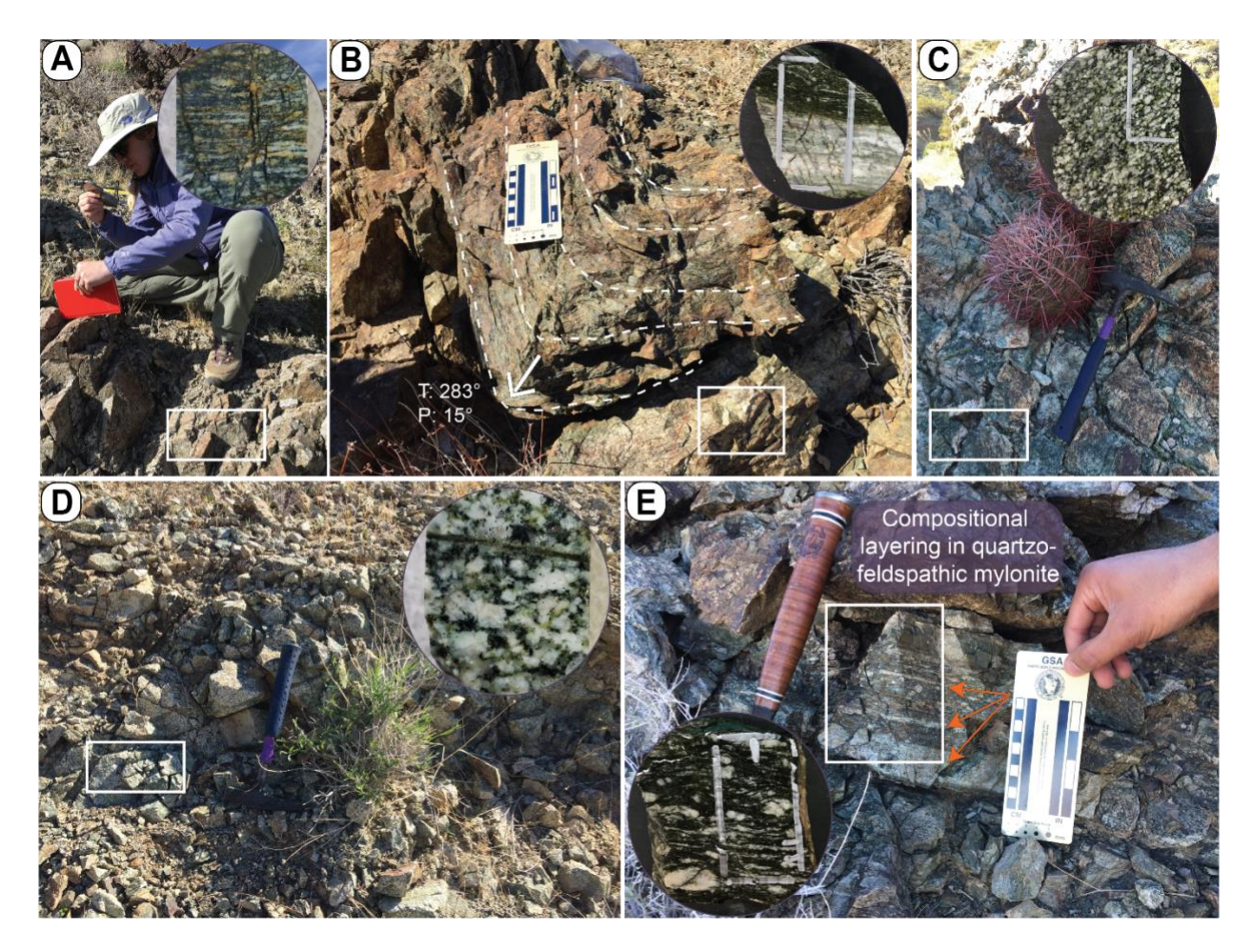
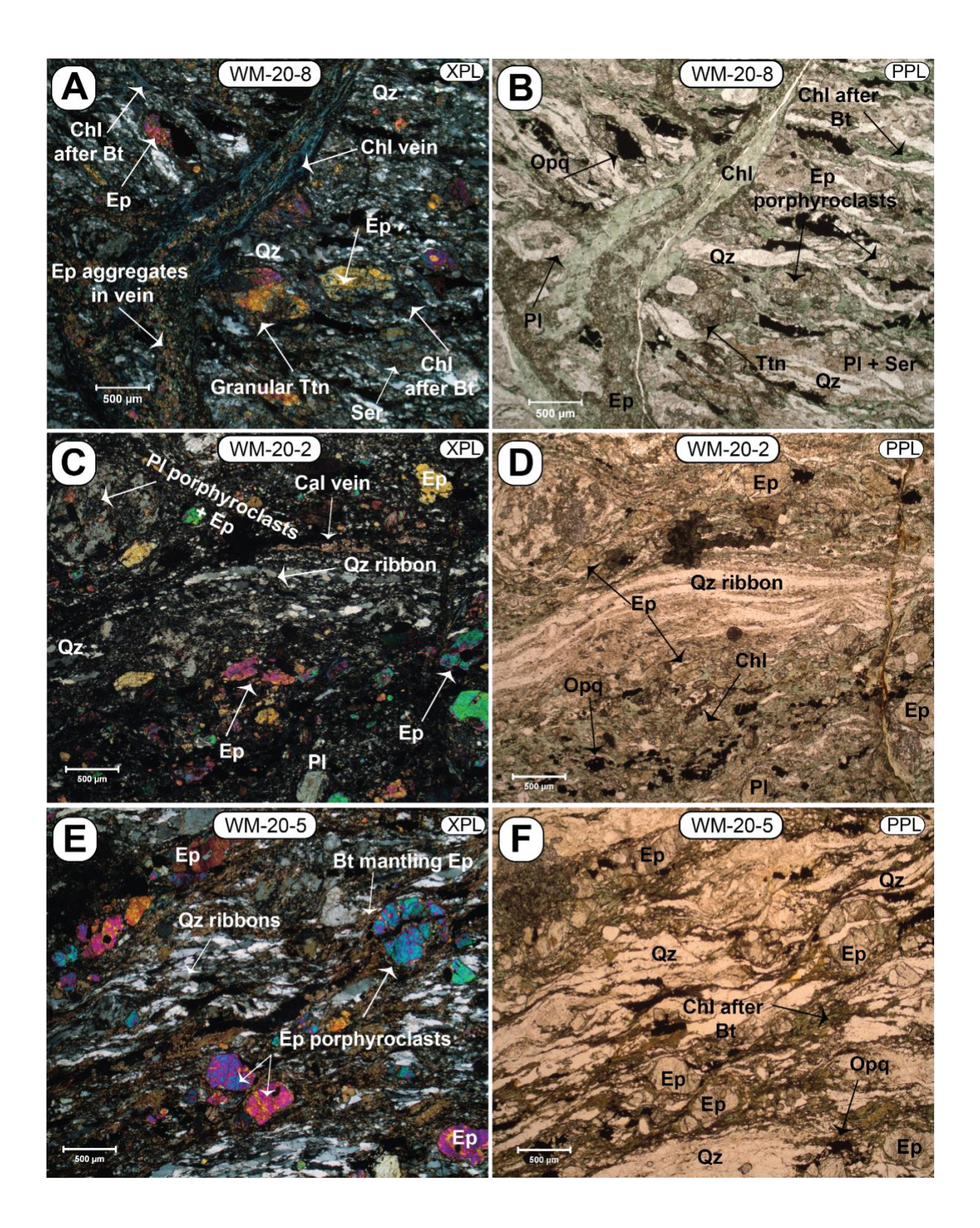


Figure 3: Field photos of samples collected at different distances below the Whipple Detachment Fault (WDF). White boxes show sampling target area. Inset circles are the resulting rock slabs showing thick section billet locations. (A) Sample WM-20-8 collected at Z_{det} <1m. (B) Sample WM-20-2 collected at Z_{det} = 6m. Folded quartz and feldspar-rich mylonite. (C) Sample WM-20-16 collected at Z_{det} = 24m. Protomylonitic biotite-epidote Cretaceous granitoid. Hammer for scale. (D) Outcrop exposure of protomylonitic Cretaceous granitoid sample WM-20-17 collected at Z_{det} = 26m. Hammer for scale. (E) Sample WM-20-5 showing distinctive mylonitic fabric collected at Z_{det} = 40m. Orange arrows point to compositional banding in the mylonite. Note: samples WM-20-2, WM-20-8, and WM-20-5 were collected along the Cupcake Mountain Trail, whereas samples WM-20-16 and WM-20-17 were collected in Bowman's Wash.



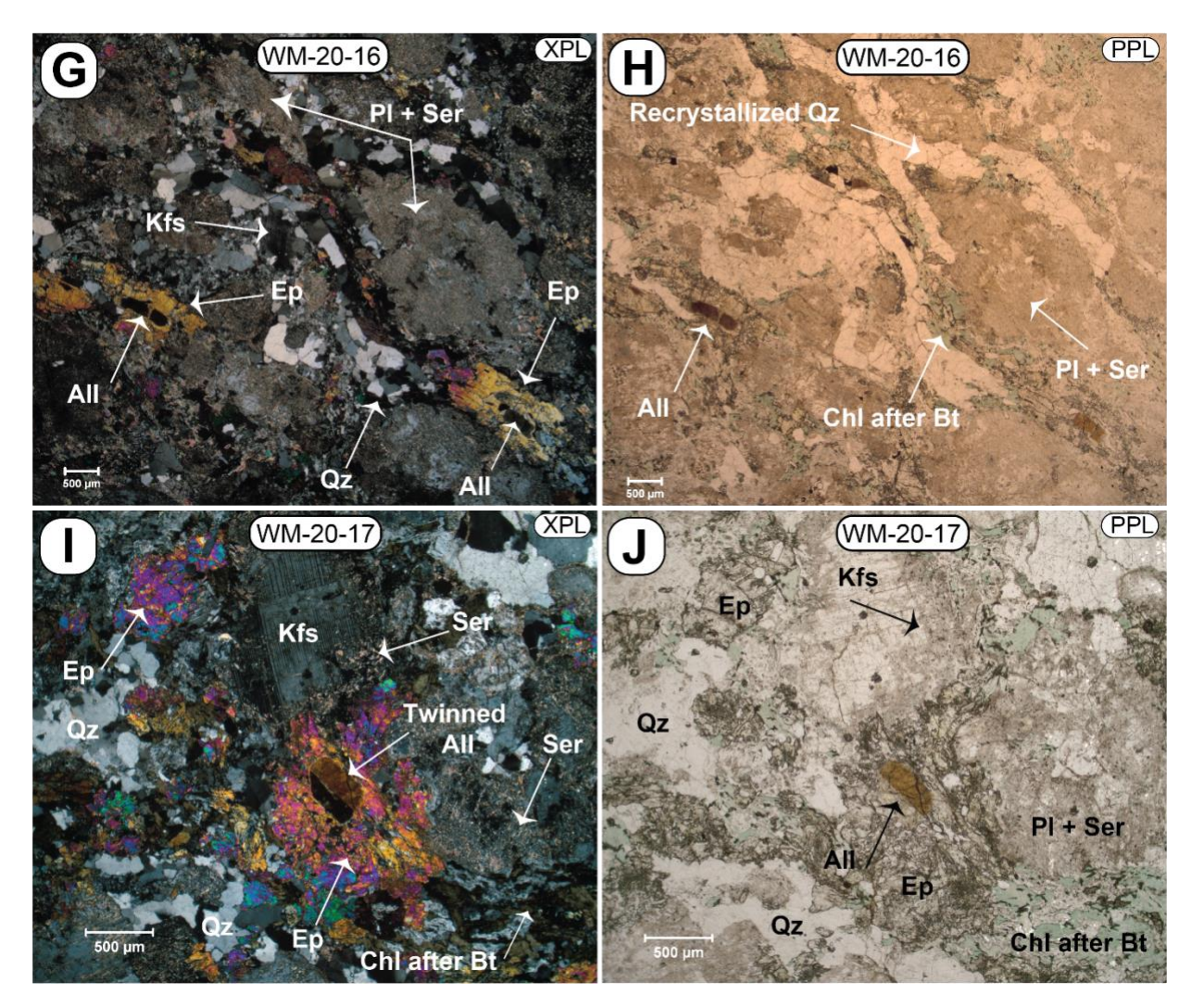


Figure 4: Photomicrographs of representative microstructures and mineral assemblages in Whipple Mountain footwall rocks. (A-F) Cross-polarized (XPL) and plane polarized (PPL) images of samples WM-20-8, WM-20-2, WM-20-5 collected along Cupcake Mountain Trail at $Z_{det} < 1$, 6, and 40 m, respectively. (G-J) XPL and PPL images of samples WM-20-16 and WM-20-17 collected along Bowman's Wash at $Z_{det} = 24$ and 26 m, respectively. Ep = epidote; All = allanite; Pl = plagioclase; Chl = chlorite; Qz = quartz; Bt = biotite; Cal = calcite; Ttn = titanite; Ser = sericite; Opq = opaque minerals; Kfs = K-feldspar.

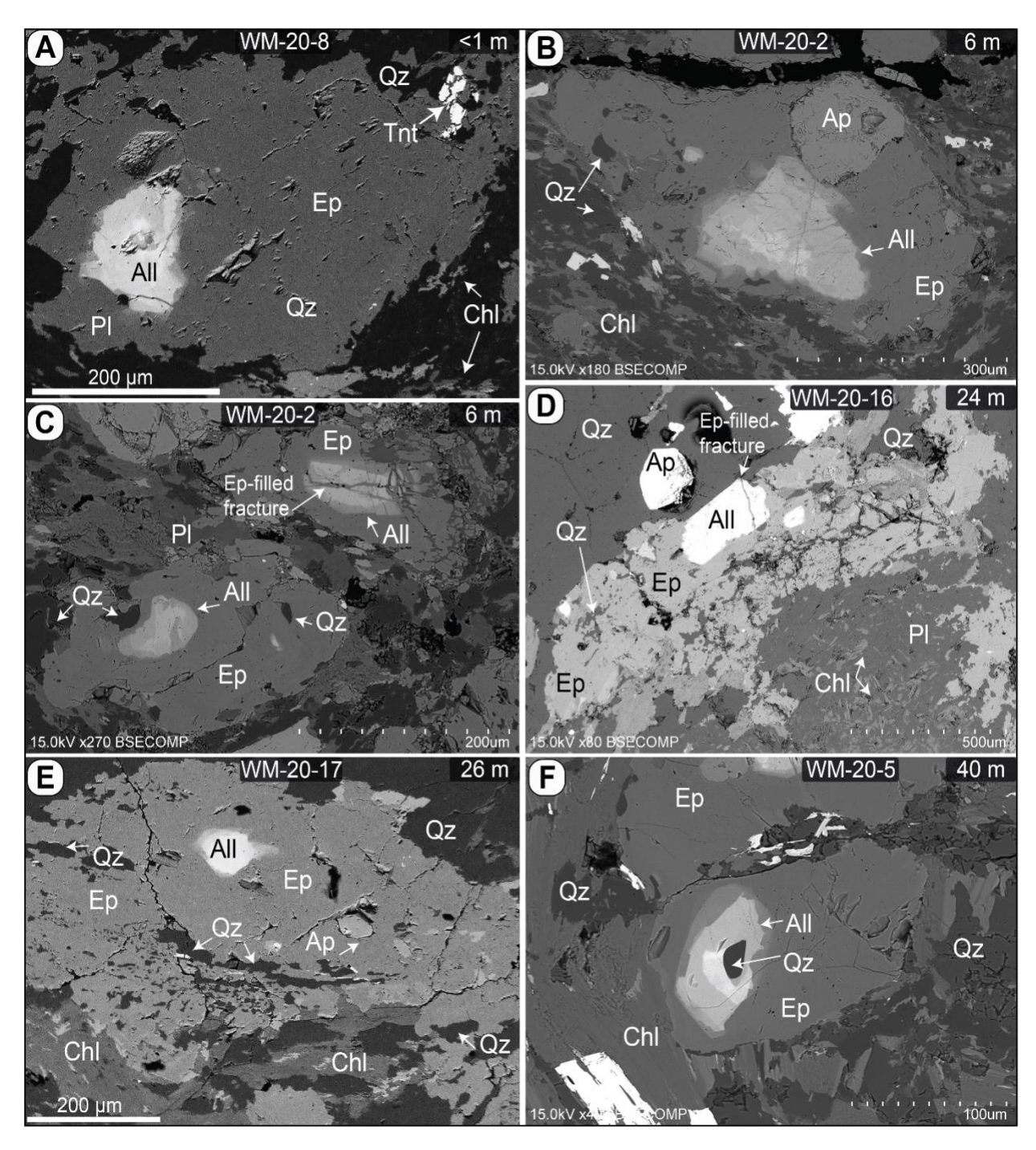


Figure 5. SEM backscattered electron images of representative quartz and epidote features and microstructures. (A) Epidote porphyrocasts from sample WM-20-8 in a recrystallized quartz + plagioclase+ chlorite matrix. (B-C) Example of epidote porphyroclasts with anhedral allanite cores in fine-grained quartz + plagioclase + chlorite matrix from sample WM-20-2. White arrow points to allanite cores in epidote porphyroclasts showing dissolution-precipitation texture. Quartz occurs as inclusions in the epidote and in the matrix (shown also by white arrows). In (B) allanite core exhibits dissolution-precipitation texture and is cross-cut by multiple fractures truncated by the epidote rim. In (C) allanite core is observed being cross-cut by epidote-filled

fractures. (D) Example of an anhedral epidote grain from sample WM-20-16 (non-mylonitic). Epidote is cross-cut by multiple quartz and chlorite-filled fratures. Allanite cores show evidence of dissolution-precipitation texture and are being cross-cut by an epidote-filled fracture. (E) Irregular epidote porphyroclast in a quartz + chlorite fine-grained matrix. Quartz and apatite inclusions are the common phases tha occur in the epidote grains. (F) Example of epidote porphyroclasts from sample WM-20-5. The matrix is dominated by quartz ribbons and biotite. Allanite core shows zoning in REE content observed by the change in BSE contrast. Ep = epidote; All = allanite; Pl = plagioclase; Chl = chlorite; Qz = quartz; Ttn = titanite; Ap = apatite.

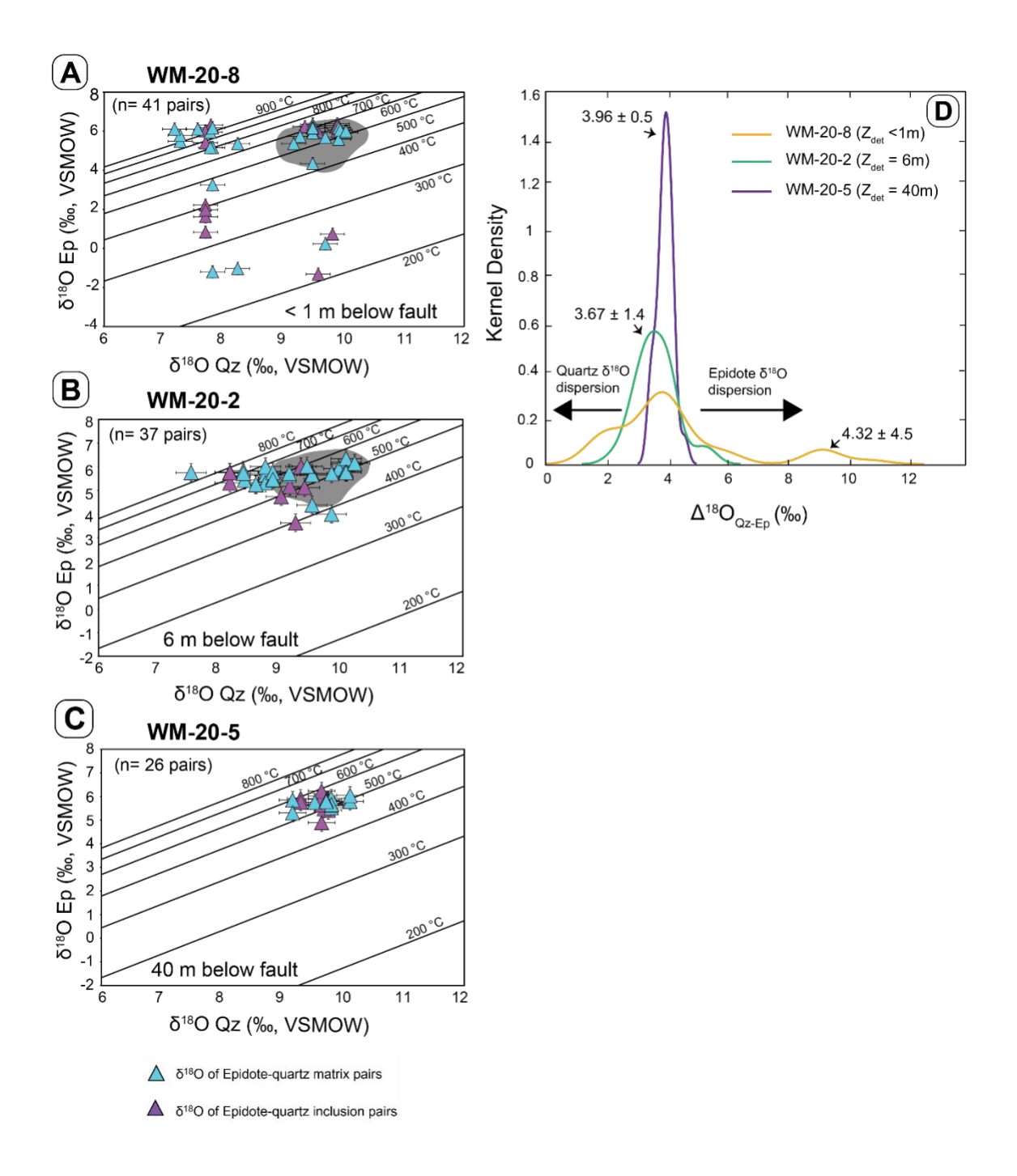


Figure 6: Plots showing oxygen isotope fractionations between quartz – epidote pairs for samples along the Cupcake Mountain Trail footwall transect. (A-C) $\delta^{18}O_{Qz}$ - $\delta^{18}O_{Ep}$ plots for assessing oxygen isotope equilibrium and temperatures between quartz and epidote pairs at Z_{det} <1m, Z_{det} = 6m, and Z_{det} = 40m. Contours are isotherms corresponding to lines of constant, equilibrium $\Delta^{18}O_{Qz-Ep}$, and thus temperature. The data cluster in C suggests oxygen isotope equilibrium. The location of the data cluster from C is outlined gray in A and B for comparison of data dispersion in samples closer to the detachment. (D) Kernel density estimate plot of the measured

fractionations for each sampled depth along the footwall transect (Supplemental Tables 3-7). Dispersion of mineral $\delta^{18}O$ values produces a spread in $\Delta^{18}O_{qz\text{-ep}}$ and systematic decrease in kernel density from the deepest sample to the shallower samples. The number of fractionation pairs for each Z_{det} distribution is shown in A-C. For comparison, mean fractionations for each Z_{det} are shown in italics beside the curves.

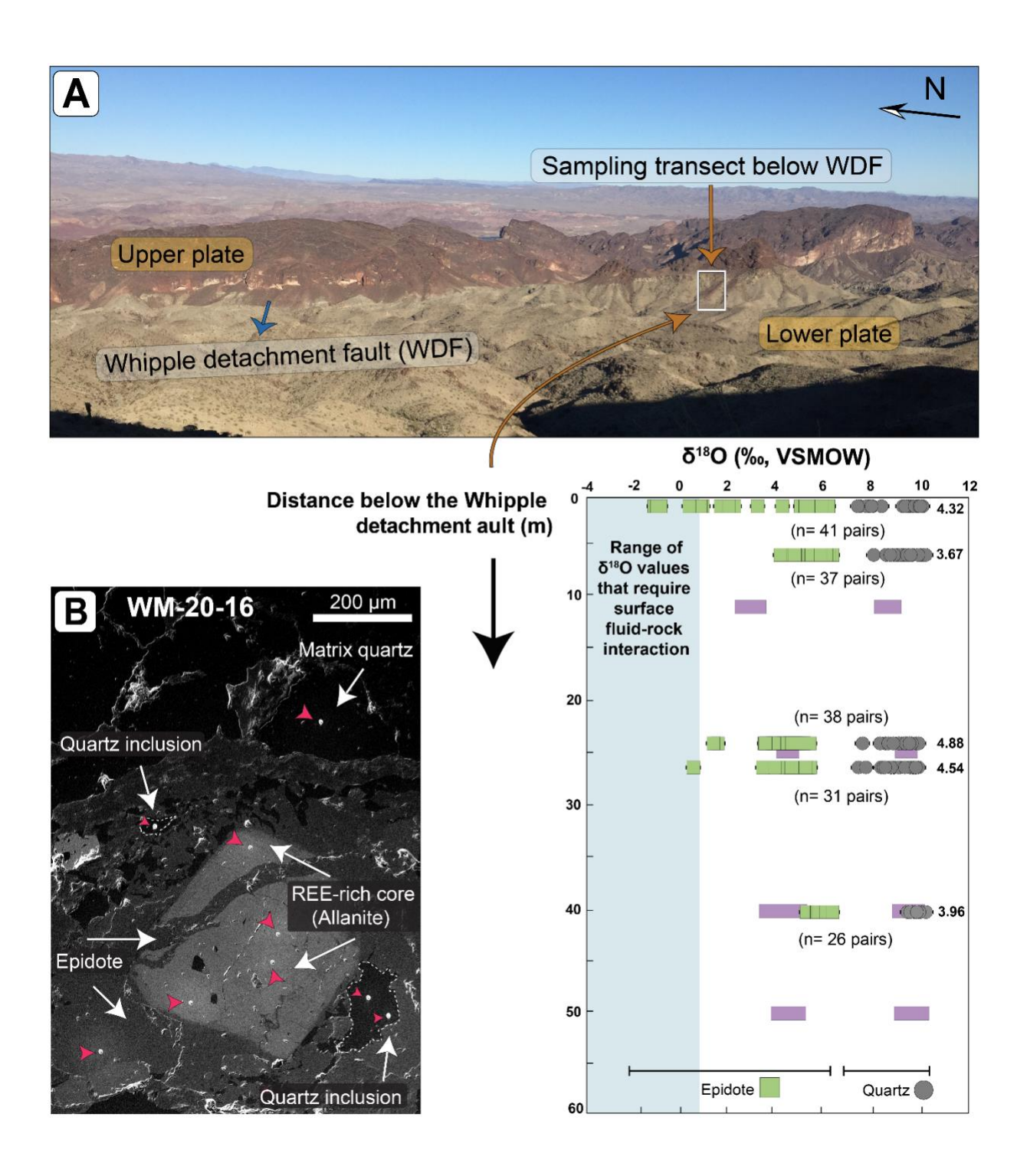


Figure 7: Whipple Mountains SIMS $\delta^{18}O$ data in spatial context. (A) $\delta^{18}O$ variability with structural distance below the WDF. Field image schematically shows a footwall traverse beneath the WDF. Colored symbols are new SIMS $\delta^{18}O$ data. For some data points, the uncertainty is smaller than the data marker symbol. Bold values on the right indicate the mean $\Delta^{18}O_{qz\text{-ep}}$ for the sample. Purple boxes show ranges for Morrison and Anderson (1998) mineral separate data. Bottom solid black bars are total epidote and quartz SIMS $\delta^{18}O$ ranges. Spread in quartz and epidote SIMS $\delta^{18}O$ decreases with distance to the main detachment fault. Low epidote $\delta^{18}O$ values require recrystallization in the presence of a meteoric fluid ($\leq 0\%$ VSMOW) (see text for discussion). (B) Secondary electron (SE) image of a target epidote porphyroclast from sample at $Z_{\text{det}} = 24\text{m}$ for SIMS analysis. Small red arrows show location of 10 μ m-diameter SIMS $\delta^{18}O$ pits. White dashed lines show the margin of quartz inclusions in the epidote grain.

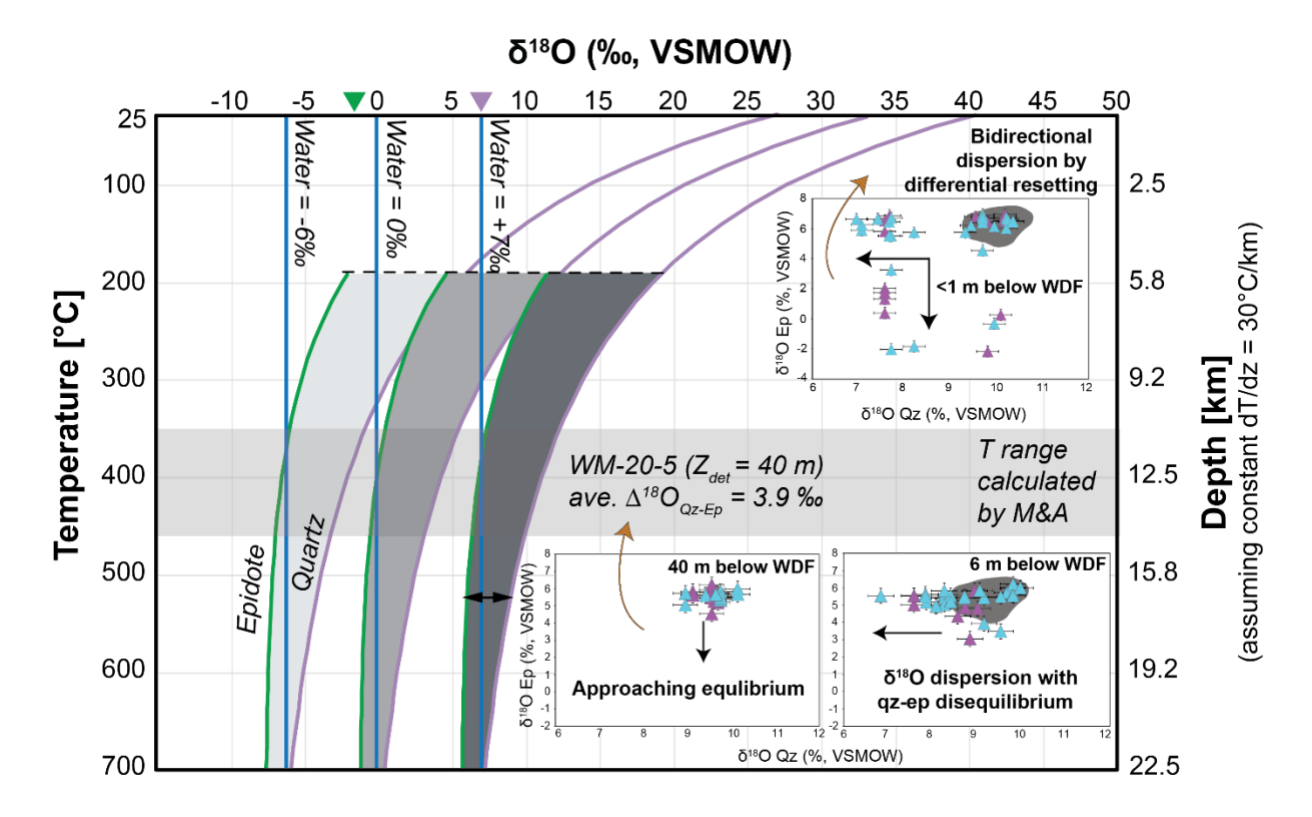


Figure 8: Equilibrium oxygen isotope fractionation models. Equilibrium quartz $\delta^{18}O$ values (purple curves) and epidote $\delta^{18}O$ values (green curves) as a function of temperature for three fixed values of water $\delta^{18}O$ (blue vertical lines) (based on epidote-H₂O of Zheng, 1993, and quartz-H₂O of Matsuhisa et al., 1979). Epidote $\delta^{18}O$ curves stop at the lower hydrothermal stability limit of epidote at ~200°C (dashed line), but quartz curves continue to surface conditions. Curves define the lowest $\delta^{18}O$ possible for quartz or epidote exchanging with water of the given $\delta^{18}O$ value. The shaded envelopes between the quartz and epidote curves show the corresponding equilibrium quartz-epidote $\delta^{18}O$ fractionations – i.e., the horizontal distance between the quartz and epidote curves is equal to the equilibrium $\Delta^{18}O_{qz\text{-ep}}$ for a given temperature. The shaded envelope slides progressively to the left with lower values of water $\delta^{18}O$ (lighter gray shading indicates isotopically lighter exchanging fluid) but maintains the same

shape. The mean $\Delta^{18}O_{qz\text{-ep}}$ from the deepest Whipple sample WM-20-5 is shown for reference. A water $\delta^{18}O \sim +7\%$ matches both the mean $\Delta^{18}O_{qz\text{-ep}}$ and the individual values of quartz $\delta^{18}O$ and epidote $\delta^{18}O$. The lowest SIMS-measured quartz $\delta^{18}O$ (purple triangle) and epidote $\delta^{18}O$ values (green triangle) in this study are shown in the top horizontal axis for reference. Representative oxygen isotope values for water were chosen based on reconstructed Miocene meteoric water (-6‰) (Gebelin et al., 2012), VSMOW/seawater (0‰), and predicted metamorphic fluid in equilibrium with the deepest Whipple sample common rock-equilibrated hydrothermal waters (+7‰). Horizontal shaded box represents the temperature range calculated in the Morrison and Anderson (1998) study from epidote-quartz $\delta^{18}O$ thermometry (using Matthews, 1994 with X_{ep} = 0.333). Simplified inset δ - δ plots correspond to the $\Delta^{18}O_{Qz\text{-Ep}}$ data from this study showing dispersion patterns at different depth below the WDF. Hypothetical depth scale shown on the right assuming a constant and elevated geotherm of 30°C/km.

Table 1. Sample location and field measurement data

Sample	Distance from WDF (m)	Lithology	UTM_X	UTM_Y	Elevation (m)	Latitude	Longitud	Strike	Dip	Trend	Plunge	Remarks
WM-20-2	~6	mylonite	11 S0746214	3804052	573	34.348567	-114.32321	075°	29°	283°	15°	foliation/ lineation
WM-20-5	~40	centimeter-scale porphyroclastic mylonite augen gneiss	11 S0746262	3804107	557	34.3490511	-114.32268	155°	40°	-	-	foliation
WM-20-8	<1	mylonitic cataclastite	11 S0746524	3804759	518	34.3548623	-114.31964	140°	41°	-	-	foliation
WM-20-16	24	bt-ep granitoid	11 S0750056	3796014	411	34.2752383	-114.28382	124°	35°	-	-	foliation/ weak fabric
WM-20-17	26	bt-ep granitoid	11 S0750090	3796007	411	34.2751671	-114.28345	083°	32°	-	-	foliation/ weak fabric

Table 1. EPMA methods and elemental data

Element /Line	Crystal	OnPeak Time	OffPeak Time	Standard	Analytical Error(rel%)	Detection Limit(99%)	Spectrometer	On-Peak Position	Backgroun d Type	Off-Peak Correction	Hi-Off Positio		Baseline
											n	n	
Na ka	LTAP	10	10	Jadeite Gates	230.547	0.020014	1	46298.2	OFF	Linear	47324	45272.2	0.45
Si ka	LTAP	10	10	Wollastonite UW	0.291819	0.019805	1	27699.6	OFF	Linear	29024	26375	0.3
Al ka	LTAP	10	10	Anorthite USNM 137041	0.358402	0.014328	1	32420.8	OFF	Linear	33646	31195.8	0.45
Mg ka	LTAP	10	10	MgO synthetic	23.1547	0.012598	1	38446.8	OFF	Linear	39572	37321.3	0.45
Fe ka	LIF	10	10	Hematite HU	2.55199	0.099807	2	48067.3	OFF	Linear	48622	47519.6	0.45
				Mn ₂ SiO ₄ (manganese olivine)									
Mn ka	LIF	10	10	synthetic	47.9615	0.101029	2	52182.3	OFF	Linear	52708	51656.7	0.45
Ca ka	LPET	10	10	Anorthite USNM 137041	0.377952	0.015234	3	38318.7	OFF	Linear	39106	37531.2	0.3
Ti ka	LPET	10	10	TiO ₂ synthetic	10.3478	0.016376	3	31346.6	OFF	Linear	32217	30476.2	0.45
La la	LPET	10	10	LaPO ₄ (USNM 168490)	-142.52	0.048844	3	30380.7	OFF	Linear	30881	29880.7	0.45
Ce la	LPET	10	10	CePO ₄ (USNM 168484)	-288.74	0.051286	3	29196	OFF	Linear	29720	28781	0.45
K ka	LPET	10	10	Microcline UW	-531.62	0.012308	5	42753.8	OFF	Linear	43502	42005.9	0.45
Y la	LPET	10	10	YPO ₄ (USNM 168499)	41.2521	0.063179	5	73769.3	OFF	Linear	74339	73199.6	0.45
Nd Ia	LIF	20	20	NdPO ₄ (USNM 168492)	-62.985	0.17479	2	58868.9	OFF	Linear	59364	58373.9	0.45
Sm la	LPET	10	10	SmPO ₄ (USNM 168494)	125.551	0.056503	5	25108.3	OFF	Linear	25488	24932.3	0.45
O ka	PC0	40	40	Anorthite USNM 137041	0.367164	0.057926	4	50428.9	OFF	Linear	54067	46790.5	0.3

Table 1. EPMA methods and elemental data cont.

Element /Line	Crystal	Windo w	Gain	Bias	Inte/Dif f	Deadtime (usec)	Takeoff	Kilovol ts	Beam Current (nA)	Beam Size (um)	Spot/S can	X Image Shift	Y Image Shift
Na ka	LTAP	4	2000	1350	INTE	3.22	40	15	20	0	Spot	0	0
Si ka	LTAP	4	1180	1350	INTE	3.22	40	15	20	0	Spot	0	0
Al ka	LTAP	4	1310	1350	INTE	3.22	40	15	20	0	Spot	0	0
Mg ka	LTAP	4	1630	1350	INTE	3.22	40	15	20	0	Spot	0	0
Fe ka	LIF	4	640	1300	INTE	3.35	40	15	20	0	Spot	0	0
Mn ka	LIF	4	670	1300	INTE	3.35	40	15	20	0	Spot	0	0
Ca ka	LPET	4	185	1850	INTE	3.3	40	15	20	0	Spot	0	0
Ti ka	LPET	4	185	1850	INTE	3.3	40	15	20	0	Spot	0	0
La la	LPET	4	180	1850	INTE	3.3	40	15	20	0	Spot	0	0
Ce la	LPET	4	180	1850	INTE	3.3	40	15	20	0	Spot	0	0
K ka	LPET	4	178	1850	INTE	3.3	40	15	20	0	Spot	0	0
Y la	LPET	4	220	1850	INTE	3.3	40	15	20	0	Spot	0	0
Nd la	LIF	4	755	1300	INTE	3.35	40	15	20	0	Spot	0	0
Sm la	LPET	4	178	1850	INTE	3.3	40	15	20	0	Spot	0	0
O ka	PC0	4	860	1480	DIFF	3.27	40	15	20	0	Spot	0	0

Table 2. Epidote mol fraction calculations based on electron microprobe analysis assuming stoichiometric oxygen of 12.5

Epidote EPMA spot analysis	Fe ³⁺ (afu)	Al ³⁺ (afu)	*X _{Ep} (mole fraction)
WM-20-5-E-S1	0.79	2.22	0.79
WM-20-5-E-S1	0.81	2.18	0.82
WM-20-5-E-S1	0.81	2.21	0.80
WM-20-5-E-S2	0.74	2.26	0.74
WM-20-5-E-S3	0.77	2.24	0.76
WM-20-5-E-S16	0.77	2.23	0.77
WM-20-5-E-S17	0.84	2.18	0.82
WM-20-5-E-S18	0.81	2.19	0.81
WM-20-5-E-S19	0.75	2.24	0.75
WM-20-5-E-S41	0.75	2.26	0.74
WM-20-5-E-S38	0.78	2.25	0.76
WM-20-5-E-S39	0.73	2.28	0.72
WM-20-5-E-S43	0.75	2.23	0.77
WM-20-5-E-S37	0.75	2.25	0.75
WM-20-5-E-S42	0.76	2.26	0.75
WM-20-5-E-S40	0.78	2.24	0.76
WM-20-5-E-S34	0.78	2.26	0.75
WM-20-5-E-S35	0.76	2.25	0.75
WM-20-5-E-S33	0.75	2.25	0.75
WM-20-5-E-S32	0.74	2.25	0.75
WM-20-5-E-S31	0.72	2.27	0.72
WM-20-5-E-S29	0.73	2.26	0.74
WM-20-5-E-S28	0.74	2.24	0.75
WM-20-5-E-S30	0.76	2.26	0.75
WM-20-5-E-S21	0.75	2.25	0.75
WM-20-5-E-S20	0.76	2.25	0.76
WM-20-5-E-S74	0.76	2.26	0.75
WM-20-5-E-S73	0.73	2.25	0.75

^{*} Mol fraction epidote (X_{Ep}) calculations are based on Fe^{3+} and Al^{3+} in atoms per formula unit (afu).

$$X_{Ep} = \frac{Fe^{3+}}{Fe^{3+} + AI - 2}$$

Franz and Liebscher (2004)

Note: Cr³⁺ was not meassured

Table 2. Epidote mol fraction calculations based on electron microprobe analysis assuming stoichiometric oxygen of 12.5 cont.

Epidote EPMA spot analysis	Fe ³⁺ (afu)	Al ³⁺ (afu)	*X _{Ep} (mole fraction)
WM-20-5-E-S71	0.77	2.21	0.79
WM-20-5-E-S72	0.74	2.25	0.75
WM-20-2-E-S12	0.78	2.22	0.78
WM-20-2-E-S13	0.76	2.24	0.76
WM-20-2-E-S21	0.84	2.18	0.82
WM-20-2-E-S5	0.76	2.24	0.76
WM-20-2-E-S3	0.82	2.16	0.83
WM-20-2-All1-S1	0.80	2.20	0.80
WM-20-2-E-S14	0.83	2.18	0.82
WM-20-2-E-S6	0.78	2.22	0.78
WM-20-2-E-S7	0.84	2.15	0.85
WM-20-2-E-S34	0.83	2.17	0.83
WM-20-2-E-S83	0.84	2.17	0.84
WM-20-2-E-S15	0.79	2.21	0.79
WM-20-2-E-S16	0.88	2.13	0.87
WM-20-2-E-S48	0.88	2.15	0.86
WM-20-2-E-S32	0.73	2.27	0.73
WM-20-2-E-S41	0.80	2.21	0.79
WM-20-2-E-S23	0.79	2.21	0.79
WM-20-2-E-S58	0.84	2.12	0.87
WM-20-2-E-S73	0.82	2.18	0.82
WM-20-2-E-S75	0.87	2.16	0.85
WM-20-2-E-S76	0.79	2.19	0.81
WM-20-2-E-S77	0.82	2.16	0.84
WM-20-2-E-S74	0.81	2.23	0.78
WM-20-2-E-S78	0.77	2.24	0.76
WM-20-2-E-S72	0.79	2.18	0.81

Table 2. Epidote mol fraction calculations based on electron microprobe analysis assuming stoichiometric oxygen of 12.5 cont.

Epidote EPMA spot analysis	Fe ³⁺ (afu)	Al ³⁺ (afu)	*X _{Ep} (mole fraction)
WM-20-2-E-S43	0.83	2.19	0.81
WM-20-2-E-S42	0.82	2.17	0.83
WM-20-2-E-S57	0.80	2.19	0.81
WM-20-2-E-S80	0.74	2.29	0.72
WM-20-2-E-S59	0.79	2.20	0.79
WM-20-2-E-S20	0.81	2.18	0.82
WM-20-2-E-S79	0.82	2.16	0.83
WM-20-2-E-S19	0.79	2.20	0.80
WM-20-2-E-S63	0.71	2.29	0.71
WM-20-2-E-S35	0.91	2.09	0.91
WM-20-2-E-S36	0.83	2.19	0.82
WM-20-2-E-S45	0.80	2.21	0.79
WM-20-2-E-S46	0.76	2.22	0.77
WM-20-2-E-S11	0.78	2.20	0.80
WM-20-16-E-S9	0.85	2.14	0.86
WM-20-16-E-S11	0.80	2.21	0.79
WM-20-16-E-S13	0.86	2.16	0.84
WM-20-16-E-S12	0.94	2.04	0.96
WM-20-16-Ev-S1	0.78	2.20	0.80
WM-20-16-Ev-S1	0.73	2.22	0.77
WM-20-16-E-S20	0.74	2.21	0.78
WM-20-16-E-S20	0.80	2.18	0.81
WM-20-16-E-S15	0.82	2.19	0.81
WM-20-16-E-S16	0.80	2.19	0.81
WM-20-16-E-S17	0.89	2.07	0.92
WM-20-16-E-S18	0.82	2.16	0.84
WM-20-16-E-S23	0.80	2.19	0.81
WM-20-16-E-S21	0.89	2.10	0.89

Table 2. Epidote mol fraction calculations based on electron microprobe analysis assuming stoichiometric oxygen of 12.5 cont.

Epidote EPMA spot analysis	Fe ³⁺ (afu)	Al ³⁺ (afu)	*X _{Ep} (mole fraction)
WM-20-16-E-S28	0.95	2.05	0.95
WM-20-16-E-S27	0.82	2.19	0.81
WM-20-16-E-S26	0.96	2.03	0.97
WM-20-16-E-S26	0.86	2.10	0.90
WM-20-16-E-S25	0.80	2.18	0.81
WM-20-16-E-S25	0.79	2.19	0.80
WM-20-16-E-S24	0.80	2.18	0.82
WM-20-16-E-S24	0.79	2.18	0.81
WM-20-16-E-S24	0.80	2.20	0.80
WM20-16-E-S33	0.82	2.17	0.83
WM20-16-E-S32	0.79	2.19	0.81
WM-20-16-E-S30	0.79	2.23	0.78
WM-20-16-E-S29	0.77	2.21	0.78
WM-20-16-E-S40	0.73	2.26	0.74
WM-20-16-E-S37	0.82	2.18	0.82
WM-20-16-E-S39	0.84	2.17	0.84
WM-20-16-E-S39	0.90	2.11	0.89
WM-20-16-E-S38	0.78	2.16	0.83
WM-20-16-E-S38	0.88	2.13	0.88
WM-20-16-E-S36	0.77	2.21	0.78
WM-20-16-E-S41	0.79	2.23	0.78
WM-20-16-E-S34	0.87	2.13	0.87
WM-20-16-E-S35	0.84	2.16	0.84
WM-20-16-E-S42	0.87	2.11	0.89
WM-20-16-E-S42	0.87	2.13	0.87
WM-20-16-E-S50	0.90	2.12	0.89
WM-20-16-E-S48	0.81	2.18	0.82
WM-20-16-E-S49	0.86	2.10	0.89

Table 2. Epidote mol fraction calculations based on electron microprobe analysis assuming stoichiometric oxygen of 12.5 cont.

Epidote EPMA spot analysis	Fe ³⁺ (afu)	Al ³⁺ (afu)	*X _{Ep} (mole fraction)
WM-20-16-E-S49	0.88	2.11	0.89
WM-20-16-E-S1	0.82	2.16	0.84
WM-20-16-E-S4	0.91	2.11	0.89
WM-20-16-E-S4	0.87	2.13	0.87
WM-20-16-E-S5	0.90	2.13	0.87
WM-20-16-E-S5	0.84	2.17	0.83
WM-20-16-E-S6	0.85	2.19	0.82
WM-20-16-E-S6	0.79	2.18	0.81
WM-20-16-E-S6	0.86	2.13	0.87
WM-20-16-E-S19	0.81	2.19	0.81
WM-20-16-Ev-S2	0.84	2.12	0.87
WM-20-16-Ev-S2	0.87	2.15	0.85
WM-20-16-E-S47	0.83	2.19	0.82
WM-20-16-E-S47	0.80	2.19	0.81
WM-20-16-Ev-S1	0.75	2.23	0.76
WM-20-8-E-S7	0.93	2.08	0.92
WM-20-8-E-S12	0.76	2.25	0.75
WM-20-8-E-S12	0.79	2.21	0.79
WM-20-8-E-S13	0.76	2.26	0.75
WM-20-8-E-S11	0.78	2.22	0.78
WM-20-8-E-S10	0.76	2.24	0.76
WM-20-8-E-S14	0.87	2.13	0.87
WM-20-8-E-S14	0.93	2.07	0.93
WM-20-8-E-S4	0.76	2.24	0.76
WM-20-8-E-S4	0.79	2.22	0.79
WM-20-8-E-S9	0.88	2.13	0.87
WM-20-8-E-S9	0.91	2.13	0.88
WM-20-8-E-S5	0.79	2.24	0.77
WM-20-8-E-S5	0.88	2.12	0.88
WM-20-8-E-S5	0.72	2.28	0.72
WM-20-8-E-S1	0.74	2.24	0.75
WM-20-8-E-S2	1.46	2.26	0.85

Table 2. Epidote mol fraction calculations based on electron microprobe analysis assuming stoichiometric oxygen of 12.5 cont.

Epidote EPMA spot analysis	Fe ³⁺ (afu)	Al ³⁺ (afu)	*X _{Ep} (mole fraction)
WM-20-8-E-S2	0.87	2.13	0.87
WM-20-8-E-S39	0.78	2.23	0.77
WM-20-8-E-S39	0.77	2.24	0.76
WM-20-8-E-S19	0.88	2.15	0.86
WM-20-8-E-S19	0.74	2.25	0.74
WM20-8-E-S19	0.75	2.25	0.75
WM20-8-E-S20	0.83	2.18	0.82
WM20-8-E-S20	0.88	2.13	0.87
WM-20-8-E-S17	0.85	2.14	0.86
WM-20-8-E-S17	0.86	2.13	0.87
WM-20-8-E-S17	0.87	2.14	0.86
WM-20-8-E-S18	0.92	2.15	0.86
WM-20-8-E-S18	0.91	2.06	0.94
WM-20-8-E-S15	0.79	2.22	0.78
WM-20-8-E-S15	0.78	2.15	0.84
WM-20-8-E-S15	0.77	2.19	0.80
WM-20-8-E-S15	0.77	2.23	0.77
WM-20-8-E-S77	0.93	2.08	0.92
WM-20-8-E-S76	0.89	2.12	0.88
WM-20-8-E-S66	0.93	2.05	0.95
WM-20-8-E-S65	0.87	2.11	0.89
WM-20-8-E-S68	0.90	2.11	0.89
WM-20-8-E-S67	0.97	2.07	0.93
WM-20-8-E-S74	0.81	2.20	0.80
WM-20-8-E-S74	0.82	2.19	0.81
WM-20-8-E-S74	0.84	2.17	0.83
WM-20-8-E-S75	0.79	2.22	0.79

Table 2. Epidote mol fraction calculations based on electron microprobe analysis assuming stoichiometric oxygen of 12.5 cont.

Epidote EPMA spot analysis	Fe ³⁺ (afu)	Al ³⁺ (afu)	*X _{Ep} (mole fraction)
WM-20-8-E-S75	0.78	2.15	0.84
WM-20-8-E-S69	0.73	2.25	0.74
WM-20-8-E-S71	0.83	2.15	0.85
WM-20-8-E-S62	0.75	2.25	0.75
WM-20-8-E-S59	0.98	2.04	0.96
WM-20-8-E-S59	0.96	2.04	0.96
WM-20-8-E-S59	0.96	2.03	0.97
WM-20-8-E-S58	0.84	2.20	0.81
WM-20-8-E-S58	0.85	2.19	0.82
WM-20-8-E-S58	0.82	2.18	0.82
WM-20-8-E-S47	0.94	2.09	0.91
WM-20-8-E-S47	0.88	2.10	0.90
WM-20-8-E-S48	0.76	2.23	0.77
WM-20-8-E-S48	0.75	2.25	0.75
WM-20-8-E-S49	0.86	2.14	0.86
WM-20-8-E-S49	0.84	2.14	0.86
WM-20-8-E-S50	0.79	2.23	0.77
WM-20-8-E-S50	0.79	2.19	0.80
WM-20-8-E-S50	0.79	2.23	0.77
WM-20-8-E-S80	0.77	2.25	0.76
WM-20-8-E-S79	0.79	2.20	0.80
WM-20-8-E-S79	0.81	2.19	0.81
WM-20-8-E-S78	0.91	2.11	0.89

Table 2. Epidote mol fraction calculations based on electron microprobe analysis assuming stoichiometric oxygen of 12.5 cont.

Epidote EPMA spot analysis	Fe ³⁺ (afu)	Al ³⁺ (afu)	*X _{Ep} (mole fraction)
WM-20-8-E-S33	0.72	2.26	0.73
WM-20-8-E-S33	0.76	2.24	0.76
WM-20-8-E-S30	0.78	2.23	0.77
WM-20-8-E-S32	0.79	2.23	0.77
WM-20-8-E-S42	0.81	2.18	0.82
WM-20-8-E-S42	0.88	2.11	0.89
WM-20-8-E-S40	0.81	2.20	0.80
WM-20-8-E-S40	0.76	2.22	0.77
WM-20-8-E-S23	0.73	2.26	0.74
WM-20-8-E-S23	0.79	2.14	0.85
WM-20-8-E-S23	0.89	2.13	0.88
WM-20-8-E-S24	0.93	2.08	0.92
WM-20-8-E-S24	0.80	2.17	0.83
WM-20-8-E-S24	0.89	2.10	0.90
WM-20-17-E-S21	0.78	2.21	0.79
WM-20-17-E-S21	0.84	2.17	0.83
WM-20-17-E-S22	0.86	2.17	0.83
WM-20-17-E-S22	0.81	2.18	0.82
WM-20-17-E-S23	0.89	2.10	0.90
WM-20-17-E-S23	0.93	2.08	0.92
WM-20-17-E-S24	0.89	2.10	0.90
WM-20-17-E-S24	0.82	2.15	0.85
WM-20-17-E-S27	0.79	2.20	0.80
WM-20-17-E-S27	0.80	2.21	0.79
WM-20-17-E-S28	0.80	2.17	0.82
WM-20-17-E-S28	0.79	2.18	0.81
WM-20-17-E-S29	0.76	2.24	0.76
WM-20-17-E-S29	0.72	2.24	0.75

Table 2. Epidote mol fraction calculations based on electron microprobe analysis assuming stoichiometric oxygen of 12.5 cont.

Epidote EPMA spot analysis	Fe ³⁺ (afu)	Al ³⁺ (afu)	*X _{Ep} (mole fraction)
WM-20-17-E-S31	0.83	2.12	0.87
WM-20-17-E-S31	0.87	2.14	0.86
WM-20-17-E-S34	0.93	2.10	0.90
WM-20-17-E-S34	0.81	2.21	0.80
WM-20-17-E-S32	0.89	2.11	0.89
WM-20-17-E-S32	0.92	2.08	0.92
WM-20-17-E-S30	0.94	2.06	0.94
WM-20-17-E-S30	0.90	2.07	0.93
WM-20-17-E-S40	0.95	2.06	0.94
WM-20-17-E-S40	0.96	2.05	0.95
WM-20-17-E-S40	0.93	2.07	0.93
WM-20-17-E-S40	0.93	2.09	0.91
WM-20-17-E-S12	0.82	2.15	0.84
WM-20-17-E-S12	0.89	2.11	0.89
WM-20-17-E-S9	0.80	2.16	0.84
WM-20-17-E-S9	0.68	2.27	0.72
WM-20-17-E-S10	0.75	2.21	0.78
WM-20-17-E-S10	0.78	2.19	0.80
WM-20-17-E-S11	0.76	2.20	0.79
WM-20-17-E-S11	0.73	2.27	0.73
WM-20-17-E-S8	0.78	2.22	0.78
WM-20-17-E-S8	0.81	2.18	0.82
WM-20-17-E-S6	0.79	2.19	0.80
WM-20-17-E-S6	0.75	2.23	0.77
WM-20-17-E-S7	0.74	2.25	0.75
WM-20-17-E-S7	0.71	2.29	0.71
WM-20-17-E-S16	0.85	2.15	0.85
WM-20-17-E-S16	0.85	2.11	0.88

Table 2. Epidote mol fraction calculations based on electron microprobe analysis assuming stoichiometric oxygen of 12.5 cont.

Epidote EPMA spot analysis	Fe ³⁺ (afu)	Al ³⁺ (afu)	*X _{Ep} (mole fraction)	
WM-20-17-E-S20	0.78	2.21	0.79	
WM-20-17-E-S20	0.85	2.14	0.86	
WM-20-17-E-S17	0.90	2.08	0.91	
WM-20-17-E-S17	0.84	2.14	0.86	
WM-20-17-E-S18	0.77	2.16	0.83	
WM-20-17-E-S18	0.82	2.16	0.84	
WM-20-17-E-S19	0.82	2.15	0.84	
WM-20-17-E-S19	0.80	2.19	0.80	
WM-20-17-E-S19	0.78	2.18	0.81	
WM-20-17-E-S43	0.82	2.19	0.81	
WM-20-17-E-S43	0.57	2.12	0.83	
WM-20-17-E-S46	0.90	2.10	0.90	
WM-20-17-E-S45	0.79	2.19	0.80	
WM-20-17-E-S45	0.78	2.20	0.80	
WM-20-17-E-S44	0.91	2.08	0.92	
WM-20-17-E-S44	0.77	2.23	0.77	
WM-20-17-E-S1	0.76	2.22	0.78	
WM-20-17-E-S1	0.77	2.24	0.76	
WM-20-17-E-S2	0.79	2.20	0.80	
WM-20-17-E-S2	0.77	2.22	0.78	
WM-20-17-E-S4	0.89	2.11	0.89	
WM-20-17-E-S4	0.81	2.18	0.81	
WM-20-17-E-S5	0.93	2.08	0.92	
WM-20-17-E-S5	0.80	2.19	0.81	
WM-20-17-E-S5	0.94	2.08	0.92	
WM-20-17-E-S5	0.82	2.16	0.84	

Table 3. Epidote & quartz mineral pairs for sample WM-20-16: 24 meter below WDF (n= 38 pairs)

Epidote SIMS spot analysis	δ ¹⁸ O ‰ VSMOW Epidote	Quartz SIMS spot analysis	δ ¹⁸ O ‰ VSMOW Quartz	Δ _{Qtz-Ep} ‰
WM20-16-E-S1	4.08	WM20-16-Qi-S2	9.62	5.54
WM20-16-E-S4	4.06	WM20-16-Qm-S9	9.34	5.27
WM20-16-E-S5	3.31	WM20-16-Qm-S9	9.34	6.03
WM20-16-E-S6	1.14	WM20-16-Qm-S9	9.34	8.20
WM20-16-E-S9	4.42	WM20-16-Qm-S15	8.66	4.24
WM20-16-E-S11	4.93	WM20-16-Qm-S15	8.66	3.73
WM20-16-E-S12	4.65	WM20-16-Qm-S13	9.27	4.62
WM20-16-E-S13	3.94	WM20-16-Qm-S13	9.27	5.33
WM20-16-E-S15	5.16	WM20-16-Qi-S14	8.34	3.17
WM20-16-E-S16	4.33	WM20-16-Qi-S14	8.34	4.00
WM20-16-E-S17	4.35	WM20-16-Qi-S14	8.34	3.98
WM20-16-E-S18	4.32	WM20-16-Qi-S15	9.72	5.40
WM20-16-E-S19	4.67	WM20-16-Qm-S28	9.43	4.76
WM20-16-E-S20	1.32	WM20-16-Qm-S28	9.43	8.11
WM20-16-E-S21	4.72	WM20-16-Qm-S37	8.89	4.17
WM20-16-E-S23	4.92	WM20-16-Qi-S16	9.36	4.44
WM20-16-E-S25	3.35	WM20-16-Qi-S17	8.11	4.77
WM20-16-E-S26	4.08	WM20-16-Qi-S17	8.11	4.03
WM20-16-E-S27	4.52	WM20-16-Qi-S22	9.05	4.53
WM20-16-E-S28	4.38	WM20-16-Qm-S40	9.61	5.23
WM20-16-E-S29	4.55	WM20-16-Qi-S24	8.45	3.91
WM20-16-E-S30	4.56	WM20-16-Qi-S24	8.45	3.89
WM20-16-E-S33 CsRes=65	4.11	WM20-16-Qi-S26	9.13	5.02
WM20-16-E-S34	4.30	WM20-16-Qm-S50	9.18	4.88
WM20-16-E-S35	4.47	WM20-16-Qm-S50	9.18	4.71
WM20-16-E-S36	4.10	WM20-16-Qi-S28	9.72	5.62
WM20-16-E-S37	4.88	WM20-16-Qi-S31	9.01	4.13
WM20-16-E-S38	3.58	WM20-16-Qi-S32	8.90	5.32
WM20-16-E-S39	3.68	WM20-16-Qi-S32	8.90	5.22
WM20-16-E-S40	4.92	WM20-16-Qi-S32	8.90	3.97
WM20-16-E-S41	3.65	WM20-16-Qm-S50	9.18	5.53
WM20-16-E-S42	3.27	WM20-16-Qm-S50	9.18	5.91
WM20-16-Ev-S1	2.75	WM20-16-Qvm-S1	9.16	6.41
WM20-16-Ev-S2	4.09	WM20-16-Qvm-S2	9.31	5.22
WM20-16-E-S48	4.53	WM20-16-Qi-S36 CsRes=66	7.37	2.84
WM20-16-E-S49	3.68	WM20-16-Qi-S36 CsRes=66	7.37	3.70
WM20-16-E-S50	4.32	WM20-16-Qm-S61	9.44	5.12
WM20-16-E-S47	4.50	WM20-16-Qm-S59	9.35	4.85
WM20-16-E-S32	4.37	WM20-16-Qm-S47	8.92	4.55
E = epidote porphyroclast		iclusions in epidote porphyroclasts	Mean Δ _{Qtz-Ep}	4.88
2m = quartz in the matrix	S = SIMS spo		2SD	2.2
zm – quanz m me mamx Ev = epidote vein		z inclusion in epidote vein	230	۷.۷

Table 4. Epidote & quartz mineral pairs for sample WM-20-5: 40 meter below WDF (n= 26 pairs)

Epidote SIMS spot analysis	δ ¹⁸ O ‰ VSMOW Epidote	Quartz SIMS spot analysis	δ ¹⁸ O ‰ VSMOW Quartz	$\Delta_{ ext{Qtz-Ep}}$ ‰
WM20-5-E-S1	5.03	WM20-5-Qi-S1	9.65	4.62
WM20-5-E-S2	5.69	WM20-5-Qi-S1	9.65	3.96
WM20-5-E-S3	5.84	WM20-5-Qi-S1	9.65	3.81
WM20-5-E-S16	5.87	WM20-5-Qm-S8	9.78	3.91
WM20-5-E-S17	5.55	WM20-5-Qm-S8	9.78	4.22
WM20-5-E-S18	5.63	WM20-5-Qm-S8	9.78	4.14
WM20-5-E-S19	5.65	WM20-5-Qm-S9	9.78	4.13
WM20-5-E-S41	5.51	WM20-5-Qi-S20	9.68	4.17
WM20-5-E-S38	5.61	WM20-5-Qi-S18	9.75	4.15
WM20-5-E-S39	5.69	WM20-5-Qi-S18	9.75	4.07
WM20-5-E-S43	5.67	WM20-5-Qi-S18	9.75	4.08
WM20-5-E-S37	5.46	WM20-5-Qi-S15	9.74	4.28
WM20-5-E-S42	5.77	WM20-5-Qi-S15	9.74	3.97
WM20-5-E-S40	5.82	WM20-5-Qi-S15	9.74	3.92
WM20-5-E-S35	5.74	WM20-5Qi-S16	9.37	3.63
WM20-5-E-S34	5.86	WM20-5Qi-S16	9.37	3.50
WM20-5-E-S31	5.37	WM20-5-Qm-S23	9.26	3.89
WM20-5-E-S30	5.81	WM20-5-Qm-S23	9.26	3.45
WM20-5-E-S28	5.73	WM20-5-Qm-S22	9.56	3.82
WM20-5-E-S33	5.76	WM20-5-Qm-S26	9.71	3.95
WM20-5-E-S32	5.79	WM20-5-Qm-S26	9.71	3.92
WM20-5-E-S21	5.97	WM20-5-Qm-S17	10.03	4.06
WM20-5-E-S20	5.77	WM20-5-Qm-S17	10.03	4.27
WM20-5-E-S73	5.85	WM20-5-Qi-S33	9.65	3.80
WM20-5-E-S74	6.12	WM20-5-Qi-S33	9.65	3.53
WM20-5-E-S71	5.94	WM20-5-Qi-S33	9.65	3.70
WM20-5-E-S72	5.64	WM20-5-Qi-S33	9.65	4.01
E = epidote porphyroclast	Qi = quartz i	nclusions in epidote porphyroclasts	Mean $\Delta_{\text{Qtz-Ep}}$	3.96
Qm = quartz in the matrix	S = SIMS sp	ot number	2SD	0.5

Table 5. Epidote & quartz mineral pairs for sample WM-20-8: <1 meter below WDF (n= 41 pairs)

Epidote SIMS spot analysis	δ ¹⁸ O ‰ VSMOW Epidote	Quartz SIMS spot analysis	δ ¹⁸ O ‰ VSMOW Quartz	Δ _{Qtz-Ep} %
WM20-8-E-S46	5.03	WM20-8-Qi-S19	7.66	2.63
WM20-8-E-S47	5.61	WM20-8-Qi-S19	7.66	2.06
WM20-8-E-S49	2.01	WM20-8-Qi-S19	7.66	5.65
WM20-8-E-S50	1.44	WM20-8-Qi-S19	7.66	6.22
WM20-8-E-S58	1.78	WM20-8-Qi-S19	7.66	5.88
WM20-8-E-S62	5.93	WM20-8-Qm-S32	9.36	3.43
WM20-8-E-S65	5.57	WM20-8-Qm-S32	9.36	3.79
WM20-8-E-S66	5.73	WM20-8-Qm-S32	9.36	3.63
WM20-8-E-S67	5.51	WM20-8-Qm-S32	9.36	3.85
WM20-8-E-S68	5.81	WM20-8-Qm-S32	9.36	3.55
WM20-8-E-S69	5.73	WM20-8-Qm-S32	9.36	3.63
WM20-8-E-S71	4.02	WM20-8-Qm-S32	9.36	5.34
WM20-8-E-S74	-1.34	WM20-8-Qi-S20	9.45	10.79
WM20-8-E-S75	5.53	WM20-8-Qi-S20	9.45	3.92
WM20-8-E-S76	5.53	WM20-8-Qm-S31	9.88	4.36
WM20-8-E-S77	5.59	WM20-8-Qm-S31	9.88	4.29
WM20-8-E-S78	5.76	WM20-8-Qi-S22	9.75	3.99
WM20-8-E-S79	5.60	WM20-8-Qi-S22	9.75	4.15
WM20-8-E-S80	5.85	WM20-8-Qi-S22	9.75	3.89
WM20-8-E-S1	5.54	WM20-8-Qm-S1	7.74	2.19
WM20-8-E-S2	4.79	WM20-8-Qm-S1	7.74	2.94
WM20-8-E-S4	5.81	WM20-8-Qi-S4	9.24	3.42
WM20-8-E-S5	0.60	WM20-8-Qi-S2	9.67	9.07
WM20-8-E-S9	4.98	WM20-8-Qm-S6	9.06	4.07
WM20-8-E-S10	5.10	WM20-8-Qm-S7	7.26	2.16
WM20-8-E-S11	5.69	WM20-8-Qm-S8	7.54	1.85
WM20-8-E-S12	5.38	WM20-8-Qm-S7	7.26	1.88
WM20-8-E-S13	5.75	WM20-8-Qm-S9	7.78	2.02
VM20-8-E-S14	4.79	WM20-8-Qm-S9	7.78	2.98
VM20-8-E-S15	-1.23	WM20-8-Qm-S9	7.78	9.00
NM20-8-E-S17	2.99	WM20-8-Qm-S9	7.78	4.79
VM20-8-E-S18	5.34	WM20-8-Qm-S11	9.16	3.82
VM20-8-E-S19	0.13	WM20-8 Qm-S13	9.56	9.43
WM20-8-E-S20	5.29	WM20-8 Qm-S13	9.56	4.27
WM20-8-E-S23	-1.07	WM20-8-Qm-S16	8.17	9.24
WM20-8-E-S24	4.98	WM20-8-Qm-S16	8.17	3.19
WM20-8-E-S30	5.74	WM20-8-Qm-S20	9.77	4.03
VM20-8-E-S32	5.19	WM20-8-Qm-S20	9.77	4.58
WM20-8-E-S33	5.69	WM20-8-Qm-S27	7.17	1.49
WM20-8-E-S39	5.88	WM20-8-Qi-S14	7.75	1.87
WM20-8-E-S40	5.95	WM20-8-Qi-S15	9.75	3.80
WM20-8-E-S42	5.65	WM20-8-Qm-S26	9.79	4.14
E = epidote porphyroclast	Qi = quartz ir	nclusions in epidote porphyroclasts	Mean Δ _{Qtz-Ep}	4.32
Qm = quartz in the matrix	S = SIMS sp		2SD	4.5

Table 6. Epidote & quartz mineral pairs for sample WM-20-17: 26 meter below WDF (n= 31 pairs)

Epidote SIMS spot analysis	δ ¹⁸ O ‰ VSMOW Epidote	Quartz SIMS spot analysis	δ ¹⁸ O ‰ VSMOW Quartz	Δ _{Qtz-Ep} ‰
WM20-17-E-S1	4.77	WM20-17-Qi-S3	7.20	2.43
WM20-17-E-S10	4.88	WM20-17-Qm-S48	9.60	4.73
WM20-17-E-S11	4.59	WM20-17-Qm-S48	9.60	5.01
WM20-17-E-S12	5.08	WM20-17-Qm-S48	9.60	4.52
WM20-17-E-S16	4.36	WM20-17-Qi-S7	8.94	4.58
WM20-17-E-S17	4.51	WM20-17-Qm-S55	8.69	4.18
WM20-17-E-S18	4.61	WM20-17-Qm-S55	8.69	4.08
WM20-17-E-S19	4.89	WM20-17-Qm-S55	8.69	3.80
WM20-17-E-S2	5.03	WM20-17-Qi-S5	8.15	3.12
WM20-17-E-S20	4.41	WM20-17-Qm-S55	8.69	4.29
WM20-17-E-S21	4.93	WM20-17-Qm-S57	9.61	4.68
WM20-17-E-S22	4.91	WM20-17-Qi-S10	7.51	2.60
WM20-17-E-S23	4.60	WM20-17-Qi-S9	8.86	4.27
WM20-17-E-S24	4.34	WM20-17-Qm-S61	8.25	3.90
WM20-17-E-S27	4.58	WM20-17-Qm-S66	9.48	4.90
WM20-17-E-S28	4.74	WM20-17-Qm-S66	9.48	4.73
WM20-17-E-S29	4.83	WM20-17-Qm-S66	9.48	4.65
WM20-17-E-S30	4.73	WM20-17-Qi-S16	8.56	3.83
WM20-17-E-S31	4.48	WM20-17-Qi-S16	8.56	4.09
WM20-17-E-S32	4.63	WM20-17-Qi-S16	8.56	3.93
WM20-17-E-S34	4.37	WM20-17-Qi-S16	8.56	4.20
WM20-17-E-S4	3.21	WM20-17-Qm-S10	9.71	6.51
WM20-17-E-S40	0.30	WM20-17-Qi-S22	8.33	8.03
WM20-17-E-S43	4.37	WM20-17-Qi-S26	9.56	5.19
WM20-17-E-S44	4.20	WM20-17-Qi-S27	9.36	5.16
WM20-17-E-S45	5.02	WM20-17-Qi-S27	9.36	4.34
WM20-17-E-S46	5.18	WM20-17-Qm-S76	9.50	4.32
WM20-17-E-S5	4.55	WM20-17-Qm-S9	9.15	4.60
WM20-17-E-S6	3.71	WM20-17-Qm-S48	9.60	5.90
WM20-17-E-S7 CsRes=71	4.39	WM20-17-Qm-S48	9.60	5.21
WM20-17-E-S8	4.77	WM20-17-Qm-S48	9.60	4.83
WM20-17-E-S9	4.98	WM20-17-Qm-S48	9.60	4.62
E = epidote porphyroclast	Qi = quartz inclusi	ions in epidote porphyroclasts	Mean Δ _{Qtz-Ep}	4.54
Qm = quartz in the matrix	S = SIMS spot nur	mber	2SD	2.1

Table 7. Epidote & quartz mineral pairs for sample WM-20-2: 6 meter below WDF (n= 37 pairs)

Epidote SIMS spot analysis	δ ¹⁸ O ‰ VSMOW Epidote	Quartz SIMS spot analysis	δ ¹⁸ O ‰ VSMOW Quartz	Δ _{Qtz-Ep} ‰
WM20-2-AII1-S1	4.83	WM20-2-Qi-S4	9.04	4.21
WM20-2-E1-S11	5.56	WM20-2-Qm-S16	8.83	3.27
WM20-2-E1-S12	5.69	WM20-2-Qm-S16	8.83	3.14
WM20-2-E1-S13	5.57	WM20-2-Qm-S16	8.83	3.26
WM20-2-E1-S14	5.30	WM20-2-Qm-S16	8.83	3.53
WM20-2-E1-S15	5.29	WM20-2-Qi-S15	8.36	3.07
WM20-2-E1-S16	5.66	WM20-2-Qi-S15	8.36	2.70
WM20-2-E1-S19	5.62	WM20-2-Qm-S20	9.45	3.83
WM20-2-E1-S20	5.57	WM20-2-Qm-S20	9.45	3.88
WM20-2-E1-S21	5.85	WM20-2-Qm-S16	8.83	2.99
WM20-2-E1-S23	5.39	WM20-2-Qm-S2	8.55	3.16
WM20-2-E1-S34	5.71	WM20-2-Qm-S11	8.54	2.83
WM20-2-E1-S35	5.47	WM20-2-Qm-S30	8.93	3.46
WM20-2-E1-S36	5.66	WM20-2-Qm-S30	8.93	3.27
WM20-2-E1-S41	5.85	WM20-2-Qi-S1	9.30	3.46
WM20-2-E1-S42	5.94	WM20-2-Qm-S3	9.90	3.96
WM20-2-E1-S43	5.99	WM20-2-Qm-S3	9.90	3.91
WM20-2-E1-S45	5.56	WM20-2-Qm-S18	9.15	3.59
WM20-2-E1-S46	5.62	WM20-2-Qm-S18	9.15	3.53
WM20-2-E1-S48	5.64	WM20-2-Qm-S13	7.84	2.20
WM20-2-E1-S57	5.78	WM20-2-Qm-S12	9.81	4.03
WM20-2-E1-S58	5.75	WM20-2-Qm-S3	9.90	4.16
WM20-2-E1-S59	5.18	WM20-2-Qi-S12	9.16	3.98
WM20-2-E1-S60	4.24	WM20-2-Qm-S21	9.71	5.47
WM20-2-E1-S63	5.41	WM20-2-Qm-S30	8.93	3.52
WM20-2-E1-S72	5.14	WM20-2-Qi-S10	9.35	4.21
WM20-2-E1-S73	6.12	WM20-2-Qm-S3	9.90	3.78
WM20-2-E1-S74	5.23	WM20-2-Qm-S6	8.70	3.47
WM20-2-E1-S75	5.67	WM20-2-Qm-S3	9.90	4.24
WM20-2-E1-S76	5.65	WM20-2-Qm-S3	9.90	4.25
WM20-2-E1-S77	5.24	WM20-2-Qm-S6	8.70	3.46
WM20-2-E1-S78	5.96	WM20-2-Qm-S5	10.02	4.06
WM20-2-E1-S79	4.54	WM20-2-Qm-S20	9.45	4.91
WM20-2-E1-S80	5.61	WM20-2-Qm-S21	9.71	4.10
WM20-2-E1-S83	5.64	WM20-2-Qi-S15	8.36	2.72
WM20-2-E-S3	3.94	WM20-2-Qi-S3	9.23	5.29
WM20-2-E-S5	5.86	WM20-2-Qm-S14	9.38	3.53
WM20-2-E-S6	5.62	WM20-2-Qm-S11	8.54	2.92
E = epidote porphyroclast	Qi = quartz inclusion	ns in epidote porphyroclasts	Mean Δ_{Qtz-Ep}	3.67
Qm = quartz in the matrix	S = SIMS spot numl	ber	2SD	1.4

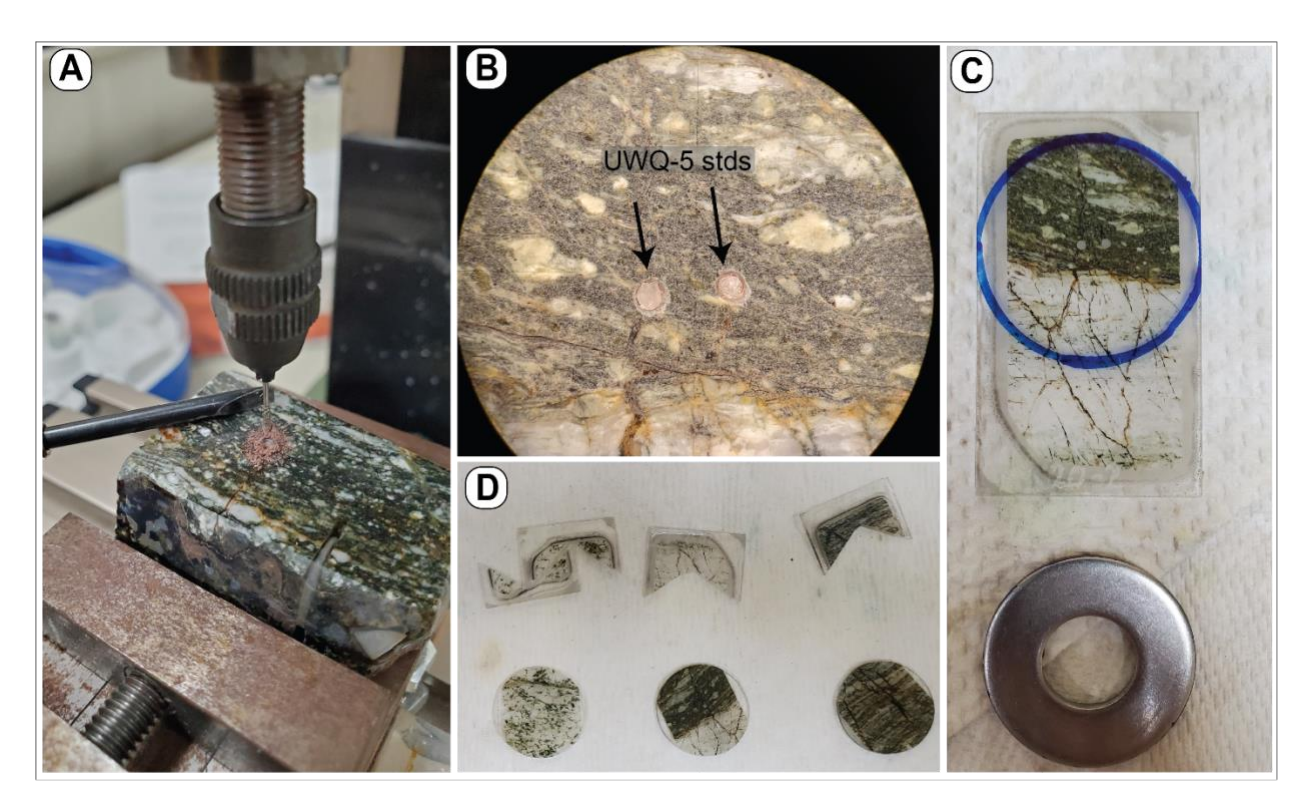


Figure S1: Thin section rounds preparation method. (A) Prior to making the thin section rounds, standard rock billets (\sim 22 mm x 40 mm) were cut from each sample slabs with a standard diamond blade saw at UW-Madison. Rock billets were drilled with a micro drill for standard grain emplacement. (B) Two shallow 2 mm diameter holes were made in each rock billet to place individual UWQ-1 standard grains (black arrows). FOV: 2 cm. (C) 100 μ m thick standard thin sections were made and later cut into 1-inch diameter rounds. (D) Thin section rounds of target areas for rock sample.

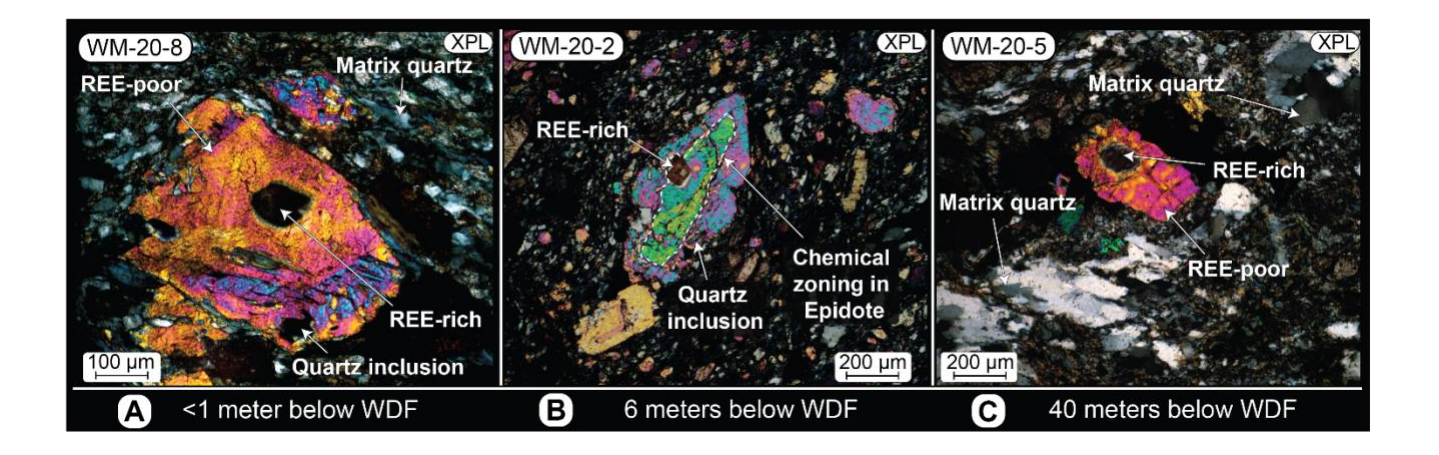


Figure S2: (A-C): Representative cross-polarized photomicrographs of epidote porphyroclasts from different structural depths. White arrows indicate different mineral textures in the samples. Images show different degrees of chemical zonation with strong interference colors, suggesting a varying Fe-Al content. Epidote-adjacent quartz in the matrix is dynamically recrystallized.

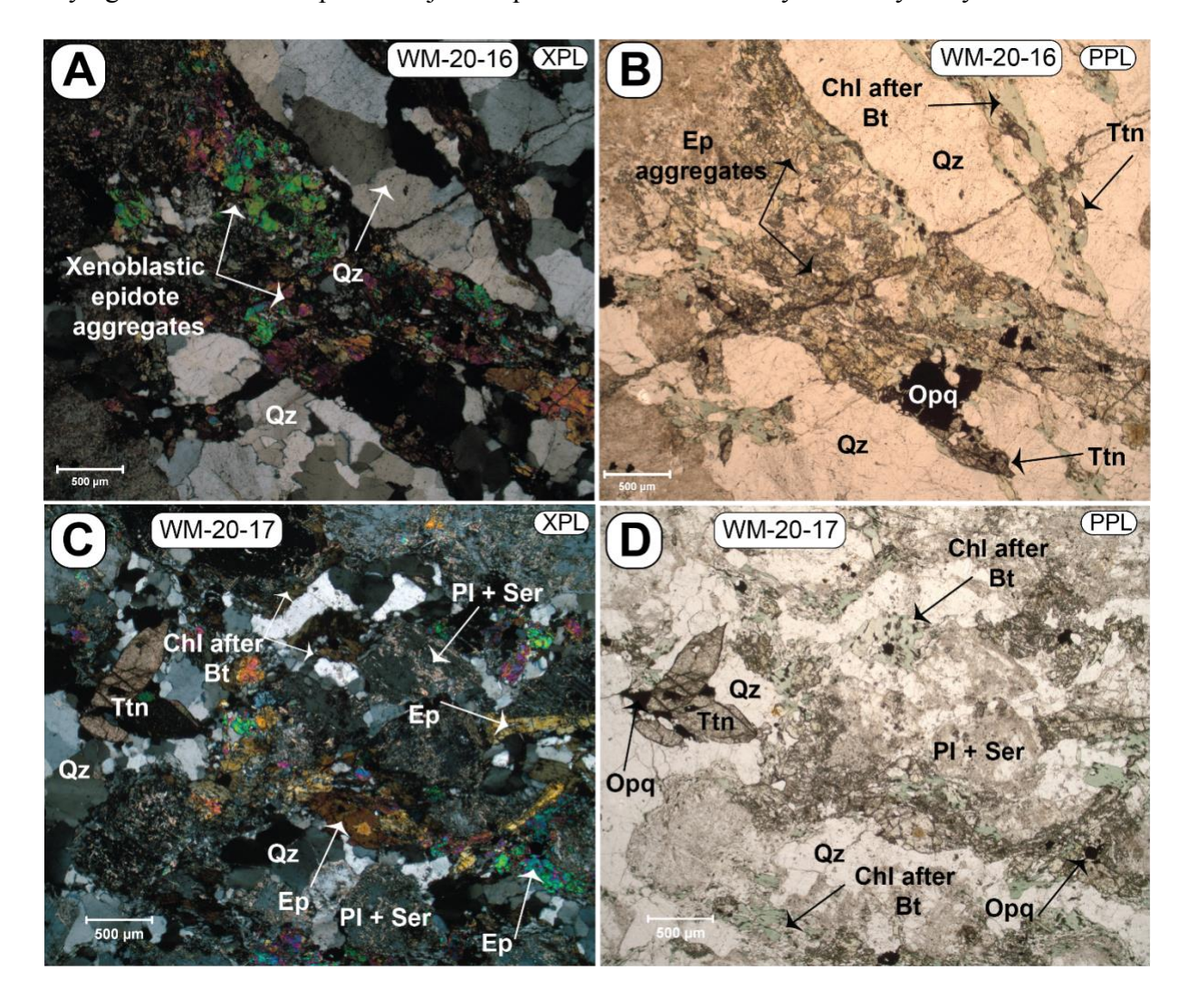


Figure S3: Cross-polarized (XPL) and plane polarized (PPL) photomicrographs of sample WM-20-16 and WM-20-17 collected along Bowman's Wash 24 meters and 26 meters, respectively below the WDF showing various protomylonitic microstructures and primary mineral phases. Ep = epidote; All = allanite; Pl = plagioclase; Chl = chlorite; Qz = quartz; Bt = biotite; Ttn = titanite; Ser = sericite; Opq = opaque minerals; Kfs = K-feldspar.

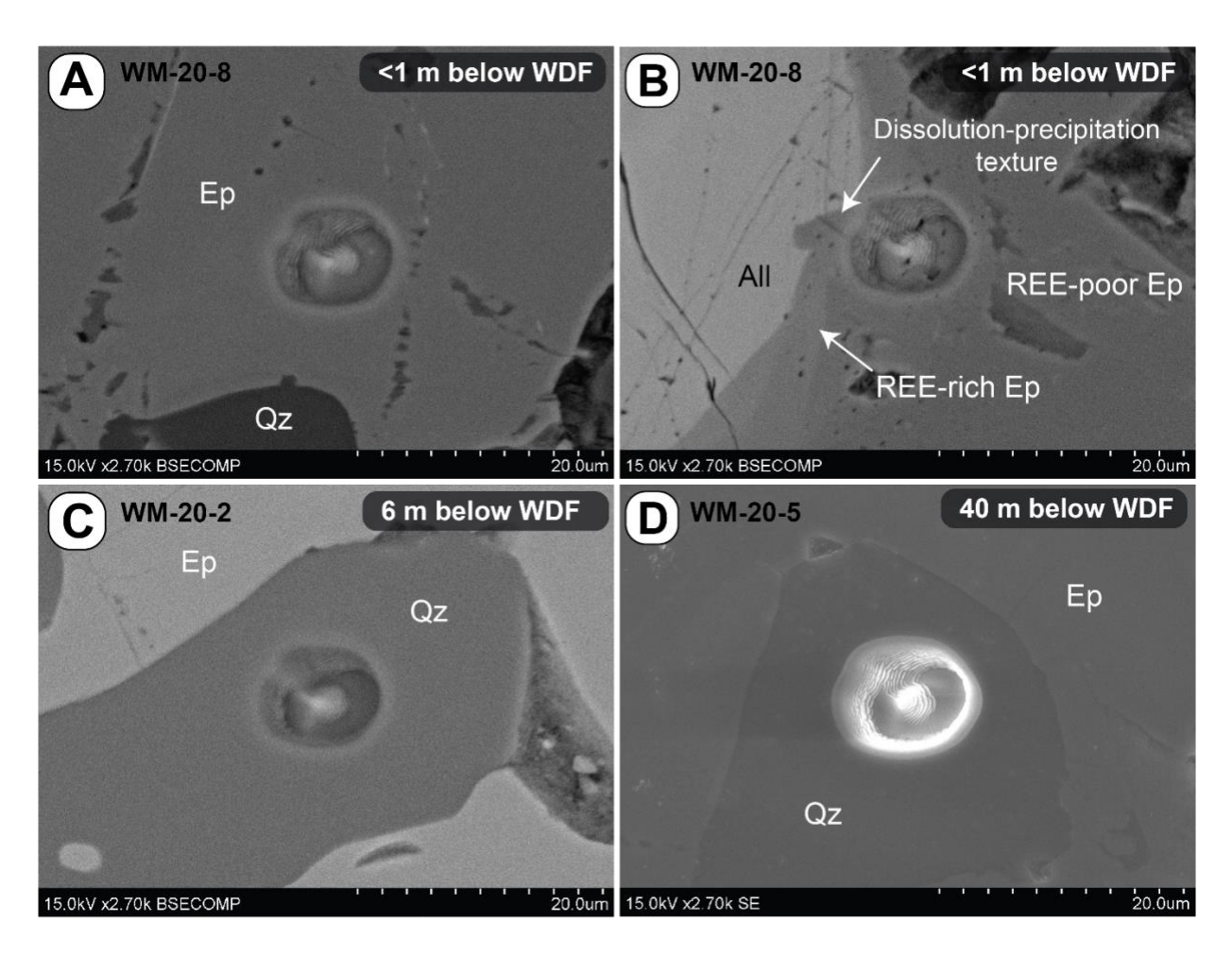


Figure S4: Post-processing SEM SIMS 10 μ m pit images of epidote porphyroclasts, quartz inclusions, and matrix quartz. Pit imaging was done to ensure quality of analytical data post SIMS analysis. Ep = epidote; All = allanite; Qz = quartz.

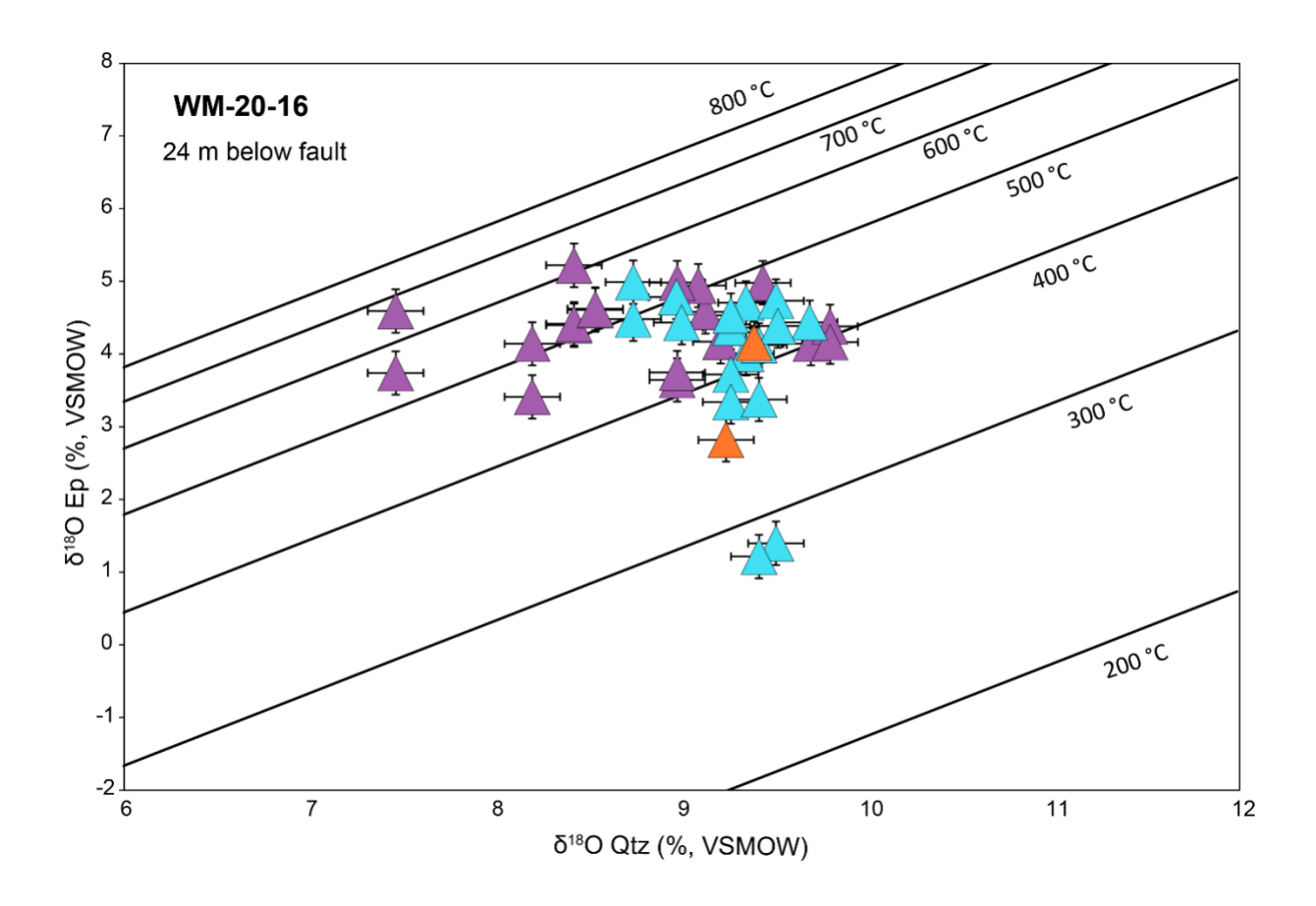


Figure S5: δ_{Qtz} - δ_{Ep} O-isotope plot of sample WM-20-16 assessing oxygen isotope equilibrium between quartz and epidote. Temperatures contours correspond to lines of constant, equilibrium ΔQtz -Ep. Purple triangles are epidote porphyroclast-quartz inclusion pairs; blue triangles are epidote porphyroclast-quartz in matrix pairs; orange triangles are epidote from vein-quartz adjacent to epidote vein pairs.

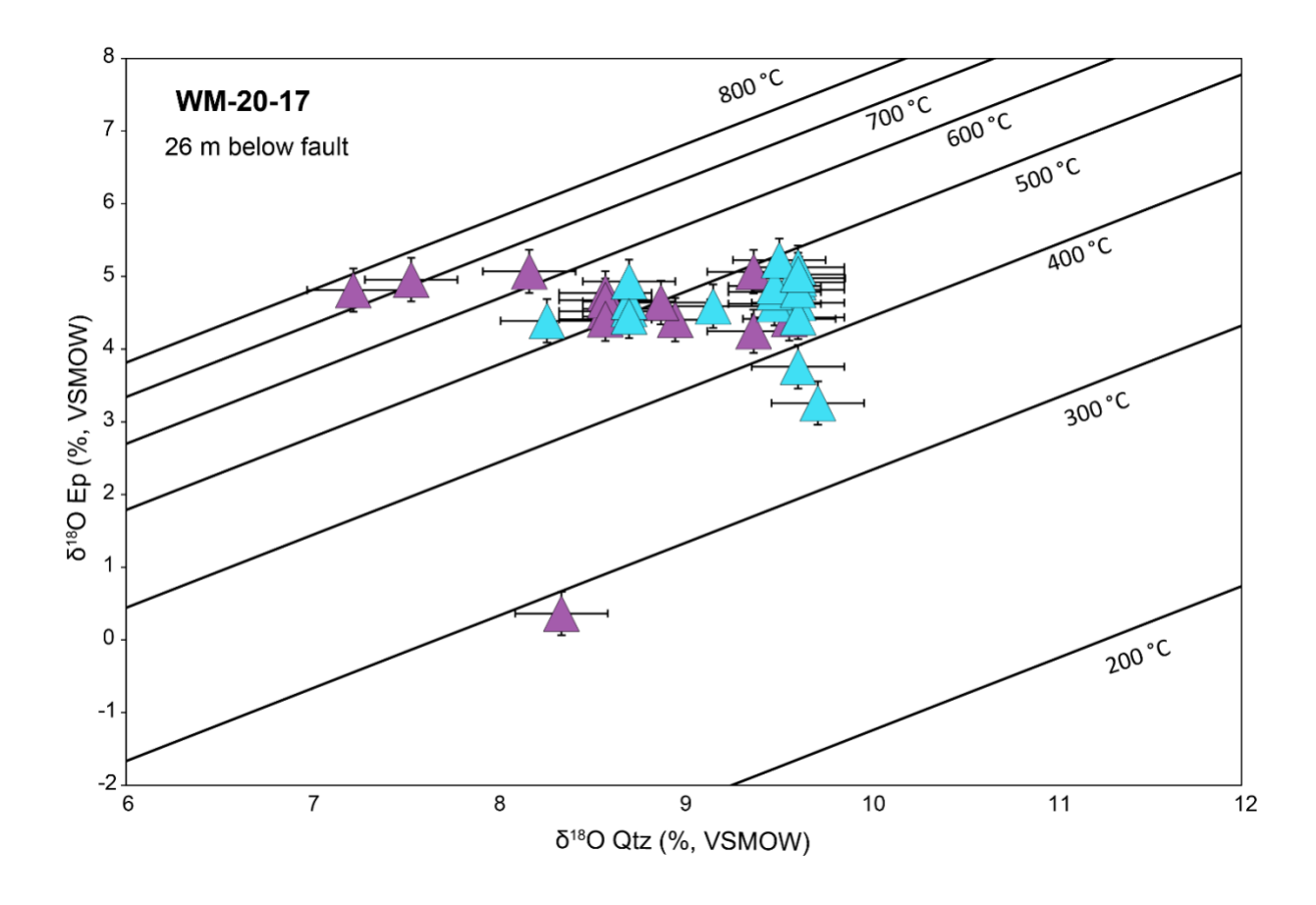


Figure S6. δ_{Qtz} - δ_{Ep} O-isotope plot of sample WM-20-17 assessing oxygen isotope equilibrium between quartz and epidote. Temperatures contours correspond to lines of constant, equilibrium ΔQtz -Ep. Purple triangles are epidote porphyroclast-quartz inclusion pairs; blue triangles are epidote porphyroclast-quartz in matrix pairs.

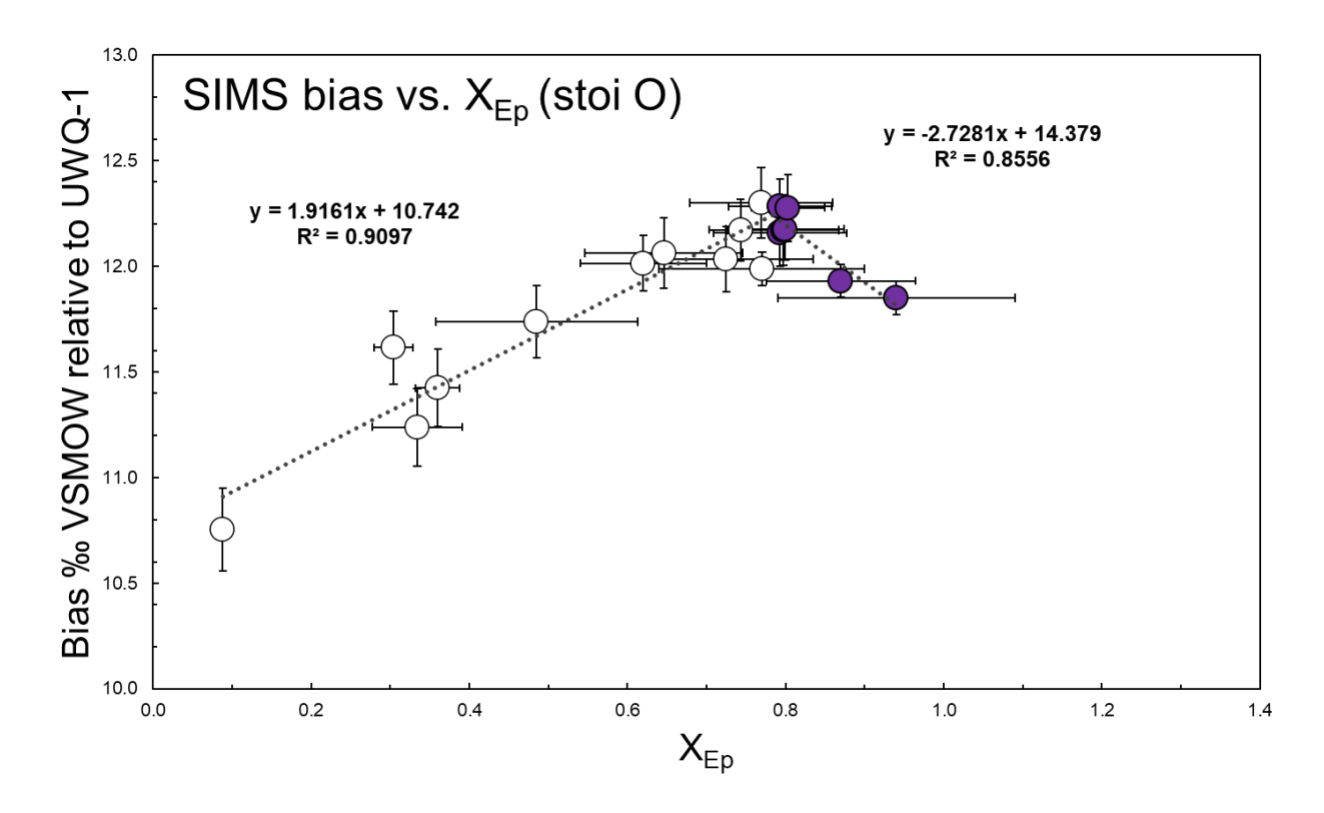


Figure S7. Piece-wise linear calibration of $\delta^{18}O$ SIMS bias relative to UWQ-1 (‰VSMOW) versus stoichiometric mole fraction X_{Ep} for epidote standards at the WiscSIMS lab (Roig González et al., 2023). Open circles are epidote standards with $X_{Ep} < 0.79$ (lower Fe content). Purple circles are epidote standards with $X_{Ep} > 0.79$ (high Fe content).

Supplemental Text

Calculation of temperatures from inferred equilibrium quartz-epidote pairs

The standard approach for calculating temperature from a mineral pair in oxygen isotope equilibrium is based on the relation

$$1000 \ln \alpha_{a-b} \approx \Delta^{18} O_{a-b} = \delta^{18} O_a - \delta^{18} O_b \approx A_{a-b} * (10^6/T^2) + B_{a-b} * (10^3/T) + C_{a-b}$$
 [eq. 1]

in which $\alpha_{a\text{-}b}$, the equilibrium oxygen isotope partition coefficient between minerals a and b, can be approximated by the functional form on the right with $A_{a\text{-}b}$, $B_{a\text{-}b}$, and $C_{a\text{-}b}$ being experimentally, empirically, or theoretically determined fractionation factors (e.g., Sharp, 2017). At high temperatures, eq. 1 can often be reduced:

$$1000 ln \alpha_{a\text{-}b} \approx \Delta^{18} O_{a\text{-}b} = \delta^{18} O_a - \delta^{18} O_b \approx A_{a\text{-}b} * (10^6/T^2) \end{eq.} \end{eq.} \end{eq.}$$

Using the measured oxygen isotope fractionation between mineral a and b, and assuming that it represents equilibrium, this equation can be solved for T, or the temperature of isotope equilibration.

In this study, we use the same empirically determined quartz-zoisite fractionation factor of Matthew (1994) for thermometry calculations as Morrison and Anderson (1998). This fractionation factor is a function not only of T but also of mole fraction epidote (X_{ep}) :

$$A_{qz-zo} = 2 + (0.75*X_{ep})$$
 [eq. 3]

Based on EPMA measurements of Whipple Mountain epidote, Xep = 0.7 and thus $A_{qz-zo} = 2.52$, was used to calculate temperatures for the samples in this study. Although not directly reported, we used temperatures supplied in Morrison and Anderson (1998) to determine that these authors used Xep = 0.33, and thus $A_{qz-zo} = 2.25$, to calculate equilibration temperatures between quartz and epidote measurements in their study.

Increasing Xep has the effect of increasing the calculated equilibration temperature. Consequently, the lower Xep used in the Morrison and Anderson (1998) study produced systematically lower temperatures than calculated from mineral pairs measured for the current study by SIMS for the Bowman's Wash samples. Applying Xep = 0.7 to the Morrison and Anderson (1998) quartz-epidote pair fractionations increases calculated equilibrium temperatures by 40-50° and produces good agreement between the uppermost temperatures calculated for Bowman's Wash samples from their mineral separate δ^{18} O data and SIMS δ^{18} O data.

- Matthews, A., 1994. Oxygen isotope geothermometers for metamorphic rocks. Journal of Metamorphic Geology 12, 211–219. https://doi.org/10.1111/j.1525-1314.1994.tb00017.x
- Morrison, J., Anderson, J.L., 1998. Footwall Refrigeration Along a Detachment Fault: Implications for the Thermal Evolution of Core Complexes. Science 279, 63–66. https://doi.org/10.1126/science.279.5347.63
- Roig González, C.I., Bonamici, C., Blum, T., Nachlas, W.O., Spicuzza, M., 2023. Epidote Reference Material Development Calibrated for Oxygen Isotope Determination by Secondary Ion Mass Spectrometry (SIMS). Microscopy and Microanalysis 29, 221–222. https://doi.org/10.1093/micmic/ozad067.098

Sharp, Z., 2017. Principles of stable isotope geochemistry, 2nd ed. Pearson.